AIDS virus-neutralizing antibody induction reciprocal to a PI3K gain-of-function disease

Hiroyuki Yamamoto[*1,2] and Tetsuro Matano[*1,3,4]

[1]AIDS Research Center, National Institute of Infectious Diseases, 4-7-1 Gakuen, Musashi-Murayama City, Tokyo 208-0011, Japan

[2]Department of Biomedicine, University Hospital Basel, Hebelstrasse 20, Basel 4031, Switzerland

[3]The Institute of Medical Science, The University of Tokyo, 4-6-1 Shirokanedai, Minato-ku, Tokyo 108-8639, Japan

[4]Joint Research Center for Human Retrovirus Infection, Kumamoto University, 2-2-1 Honjo, Kumamoto 860-0811, Japan

*Correspondence:

Hiroyuki Yamamoto, AIDS Research Center, National Institute of Infectious Diseases, 4-7-1 Gakuen, Musashi-Murayama City, Tokyo 208-0011, Japan. Phone: +81-42-848-7154; Fax: +81-42-848-7155. Email: h-yamato@niid.go.jp

Tetsuro Matano, AIDS Research Center, National Institute of Infectious Diseases, 1-23-1 Toyama, Shinjuku-ku, Tokyo 162-8640, Japan. Phone: +81-3-4582-2811; Fax: +81-3-5285-1165. Email: tmatano@niid.go.jp

Running title: SIV neutralization post-PI3K diminution

Abstract

HIV and simian immunodeficiency virus (SIV) infections are known for impaired neutralizing antibody (NAb) responses. While sequential virus-host B cell interaction appears to be basally required for NAb induction, driver molecular signatures predisposing to NAb induction still remain largely unknown. Here we describe SIV-specific NAb induction following a virus-host interplay reciprocal to a congenital human antibody-deficient disease. Screening of seventy neutralization-resistant SIV_{mac239}-infected macaques found nine NAb-inducing animals, with seven selecting for a specific $CD8^+$ T-cell escape mutation in viral *nef* before NAb induction. This mutation reduced aberrant Nef interaction-mediated drive of B-cell maturation-limiting phosphoinositide 3-kinase (PI3K)/mammalian target of rapamycin complex 2 (mTORC2). *In vivo* imaging cytometry depicted preferential Nef perturbation of cognate Envelope-specific B cells, corroborating cognate B-cell maturation post-mutant selection up to NAb induction. Results exemplify a NAb induction pattern extrinsically reciprocal to human PI3K gain-of-function antibody deficiency, shaped through two-front, sequential virus interaction with both wings of adaptive immunity.

Keywords

neutralizing antibody; B cells; $CD8^+$ T cells; PI3 kinase; inborn errors of immunity; HIV/SIV

Graphical Abstract

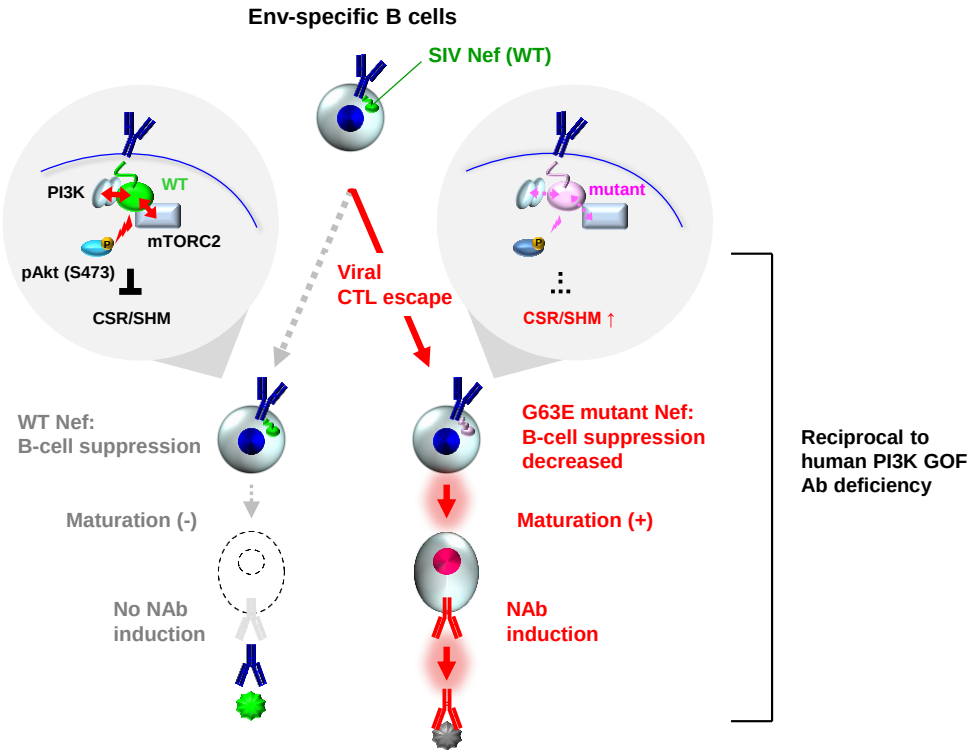

Introduction

Virus-specific neutralizing antibody (NAb) responses by B cells are induced by a tight cooperation of adaptive immune cells (Kumar et al., 2010; Shulman et al., 2014; Giltin et al., 2014; Wang et al., 2014) and often play a central role in clearance of acute viral infections (Junt et al., 2007). In contrast, persistence-prone viruses such as human immunodeficiency virus type 1 (HIV-1), simian immunodeficiency virus (SIV) and lymphocytic choriomeningitis virus (LCMV) variously equip themselves with B cell/antibody-inhibitory countermeasures (Moir et al., 2001; Mattapallil et al., 2005; Sommerstein et al., 2015; Sammicheli et al., 2016; Fallet et al., 2016; Mason et al., 2016) and NAb responses are impaired (Levesque et al.,2009; Mikell et al., 2011). These viruses successfully suppress elicitation of potent NAb responses particularly in acute infection (Hunziker et al., 2003; Tomaras et al., 2008) and establish viral persistence, posing considerable challenge for developing protective strategies.

Reciprocal to this detrimental acute-phase NAb absence, we and others have previously described that acute-phase passive NAb infusion can trigger an endogenous T-cell synergism resulting in robust SIV/SHIV (simian/human immunodeficiency virus) replication control (Haigwood et al., 1996; Yamamoto et al., 2007; Ng et al., 2010; Iseda et al., 2016; Nishimura et al., 2017). This shows that virus-specific NAbs not only confer sterile protection but also can evoke T-cell-mediated non-sterile viral control, suggesting the importance of inducing endogenous NAb responses during an optimal time frame as well as humoral-cellular response synergisms. Therefore, identifying mechanisms driving NAb induction against such viruses is an important step to eventually design NAb-based HIV control strategies.

As an approach, analysis of *in vivo* immunological events linked with NAb induction against difficult-to-neutralize SIVs in a non-human primate model can provide important insights into this goal. HIV-specific NAb induction patterns and correlates, such as antibody-NAb coevolution (Moore et al., 2012), autoimmune-driven induction (Moody et al., 2016) and natural killer cell-related host polymorphisms (Bradley et al., 2018) have been variously reported to date; the wealth of knowledge on this topic collectively, and interestingly, rather

suggests that pathways to NAb induction against neutralization-resistant viruses including HIV/SIV can be highly redundant and there may be as-yet-unknown *in vivo* mechanisms that can robustly drive NAb induction. For example, the neutralization resistance of certain SIV strains apparently is not explanatory by the aforementioned, posing such models as attractive analytic targets of NAb induction mechanisms.

In the present study, we examined virus-specific antibody responses in rhesus macaques infected with a highly neutralization-resistant SIV strain, SIV_{mac239}. This virus is highly pathogenic, shows persistent viremia and hosts lack NAb responses throughout infection (Kestler et al., 1991). Yet, upon performing a large-scale screening of SIV_{mac239}-infected rhesus macaques for up to 100 weeks, we noticed a subgroup inducing NAbs in the chronic phase. Interestingly, these animals commonly selected for a specific $CD8^+$ cytotoxic T lymphocyte (CTL) escape mutation in the viral Nef-coding gene before NAb induction. The mutant Nef, compared with wild-type (WT) Nef, manifested a decrease in aberrant interaction with phosphoinositide 3-kinase (PI3K)/mammalian target of rapamycin complex 2 (mTORC2), resulting in decreased downstream hyperactivation of the canonical B-cell negative regulator Akt (Omori et al., 2006; Limon et al., 2014). Nef was graphically identified via machine learning-comprising imaging cytometry to preferentially target Env-specific B cells *in vivo*, and in those macaques inducing NAbs, the NAb induction was linked with sustained Env-specific B-cell responses after the mutant Nef selection. Results describe a B-cell functional boosting reciprocal to human PI3K gain-of-function antibody deficiency disease, and suggest that intervening PI3K/mTORC2 signaling can potentially result in harnessing NAb induction against difficult-to-neutralize viruses.

Results

Identification of macaques inducing SIV_{mac239}-neutralizing antibodies

We performed a retrospective antibody profile screening in rhesus macaques infected with NAb-resistant SIV_{mac239} (*n* = 70) (**Figure 1A**) and identified a group of animals inducing anti-SIV_{mac239} NAb responses (*n* = 9), which were subjected to characterization. These NAb inducers showed persistent viremia with no significant difference in viral loads compared with a profile-clarified naïve, major histocompatibility complex class I (MHC-I) haplotype-balanced subgroup of NAb non-inducers (*n* = 19) representatively utilized for comparison hereafter (**Figure 1B** and **Figure 1-figure supplement 1**). Plasma SIV_{mac239}-NAb titers measured by 10 $TCID_{50}$ SIV_{mac239} virus-killing assay showed an average maximum titer of 1:16, being induced at an average of 48 weeks post-infection (p.i.) (**Figure 1C**). Two of the nine NAb inducers showed detectable NAb responses before six months p.i., while the remaining seven induced NAbs after six months. Anti-SIV_{mac239} neutralizing activity was confirmed in immunoglobulin G (IgG) purified from plasma of these NAb inducers (**Figure 1-figure supplement 2**). SIV Env-binding IgGs developed from early infection in NAb inducers as well as NAb non-inducers (**Figure 1-figure supplement 3**); titers were not higher but rather lower at year 1 p.i. in the NAb inducers (**Figure 1-figure supplement 3B** and **3C**), consistent with other reports (Havenar-Daughton et al., 2016). NAb inducers and non-inducers showed similar patterns of variations in viral *env* sequences (Burns et al., 1993), mainly in variable regions 1, 2 and 4 (V1, V2 and V4) (**Figure 1-figure supplement 4**).

Selection of a viral *nef* mutation (Nef-G63E) precedes chronic-phase SIV_{mac239}-specific NAb induction

Viral nonsynonymous polymorphisms outside *env* were next assessed. Strikingly, we found selection of a viral genome mutation resulting in G (glycine)-to-E (glutamic acid) substitution at residue 63 of Nef (Nef-G63E) in seven of the nine NAb inducers (**Figure 2A**). This 63rd residue is in the unstructured N-terminus of Nef, flanked by conserved α-helices

(**Figure 2B**). This region is conserved in HIV-2/SIV but not in HIV-1, occasionally being deleted in laboratory HIV-1 strains (Geyer et al., 2001). AlphaFold2-based structure prediction did not derive palpable change except for low-probability disruption of the alpha helices (data not shown). The Nef G63E mutation was not observed in two early NAb inducers (with detectable NAbs before 6 months p.i.) but selected in all of the remaining seven inducing detectable NAb responses after 6 months. In contrast, this mutation was found only in two of the nineteen NAb non-inducers, including one rapid progressor (**Figure 1-figure supplement 1**) and selection was significantly enriched in the NAb inducers (**Figure 2C**). Analysis of Nef-G63E mutation frequencies in plasma viruses showed that Nef-G63E selection preceded or at least paralleled NAb induction (**Figure 2D**).

Nef-G63E is a CD8$^+$ T-cell escape mutation

These seven NAb inducers selecting this mutation elicited CD8$^+$ T-cell responses specific for a 9-mer peptide Nef$_{62–70}$ QW9 (QGQYMNTPW) (**Figure 3A**). This Nef$_{62–70}$ QW9 epitope is restricted by MHC-I molecules Mamu-B*004:01 and Mamu-B*039:01 (Evans et al., 1999; Sette et al., 2012). Possession of these accounted for six cases of Nef-G63E selection (**Figure 3A**), and the remaining one animal possessed Mamu-A1*032:02 predicted to bind to Nef$_{63–70}$ GW8 (NetMHCpan). Ten of nineteen NAb non-inducers also had either of these alleles (**Figure 1-figure supplement 1**), indicating that NAb induction is not associated with these MHC-I genotypes (P = 0.25 by Fisher's exact test, data not shown) but with the Nef-G63E mutation itself (**Figure 2C**). Nef-G63E was confirmed to be an escape mutation from Nef$_{62-70}$-specific CD8$^+$ T-cell responses (**Figure 3B**). NAb non-inducers possessing these alleles elicited little or no Nef$_{62-70}$-specific CD8$^+$ T-cell responses (**Figure 3-figure supplement 1A**), suggesting that *in vivo* selection and fixation of this Nef-G63E SIV was indeed Nef$_{62-70}$-specific CD8$^+$ T cell-dependent. Replication kinetics of SIV carrying the Nef-G63E mutation was comparable with wild-type (WT) on a cynomolgus macaque HSC-F CD4$^+$ T-cell line (Akari et al., 1996), stating that the mutation does not critically impair viral replication (**Figure 3-figure supplement 1B**), and plasma viral loads were comparable between Nef-G63E mutant-

154 selecting NAb inducers versus non-inducers (**Figure 3-figure supplement 1C**). These
155 somewhat contrasted conditional reversion of a more replication-impairing *nef* mutation
156 related with CD3 downregulation loss in SIV_{mac239} infection (Joas et al., 2020). These results
157 indicate NAb induction following *in vivo* selection and fixation of the $CD8^+$ T-cell escape *nef*
158 mutation, Nef-G63E.
159
160 **G63E mutation reduces aberrant Nef interaction-mediated drive of PI3K/mTORC2**
161 We next focused on the functional phenotype of this highlighted Nef-G63E mutant SIV
162 in infected cells. An essence of host perturbation by Nef is its wide-spectrum molecular
163 downregulation, ultimately increasing viral replication (Schindler et al., 2004; Zhang et al.,
164 2009). To address possible amelioration, we compared downregulation of major targets CD3,
165 CD4, MHC-I, CXCR4 and BST-2 (Jia et al., 2009) in infected HSC-F cells. Nef-G63E mutation
166 did not confer notable change compared with wild-type (WT) [*P* = not significant (*n.s.*) for all
167 molecules, data not shown], implicating other non-canonical changes (**Figure 4A**). Literature
168 suggested ferritin negative influence on B cells proportionate to HIV-infected macrophage-
169 derived production (Swingler et al., 2008). Here, plasma ferritin showed no differences (**Figure**
170 **4-figure supplement 1A**) and viral loads were comparable between Nef-G63E-selecting NAb
171 inducers and non-inducers (**Figure 4-figure supplement 1B** and **1C**), arguing against gross
172 involvement of ferritin as well as other viral replication-changing Nef phenotypes at least in
173 this model.
174 Thus, we took interest in immunosignaling-modulating properties of Nef-G63E SIV.
175 Analysis of Akt, the predominant immune-intrinsic negative brake of B-cell maturation and
176 AFC/antibody responses *in vivo* (Omori et al., 2006; Limon et al., 2014; Fruman et al., 1999;
177 Ray et al., 2015; Sander et al., 2015), revealed that its serine 473 phosphorylation, non-
178 canonically known for Nef-mediated upregulation (Kumar et al., 2016), was significantly lower
179 on day 3 after Nef-G63E SIV infection at low multiplicity of infection (MOI) compared with WT
180 (**Figure 4B**), stronger than histogram deviation levels in PI3K gain-of-function mice with full
181 disease phenotype (Avery et al., 2018). The threonine 308-phosphorylated Akt (pAkt Thr308)

level was more unaffected (**Figure 4-figure supplement 1B**).

We further assessed properties of serine 473-phoyphorylated Akt (pAkt Ser473) inhibition by Nef-G63E SIV, and found that external PI3K stimuli (serum starvation) (Kennedy et al., 1997) accelerated phenotype appearance from day 3 to day 1 post-infection (**Figure 4C**, left). A similar trend was obtained by short-term PI3K stimulation with interferon-γ (Nguyen et al., 2001), interleukin-2 (Marzec et al., 2008) and SIV Env (François & Klotman, 2003) (**Figure 4-figure supplement 1C**). Env-stimulating high-MOI infection also accelerated phenotype appearance, with enhanced 50% reduction (**Figure 4C**, right). These showed that the Akt-inhibitory G63E mutant Nef phenotype is PI3K stimuli-dependent. Transcriptome analysis signatured decrease in PI3K-pAkt-FoxO1-related genes in mutant SIV infection (**Figure 4-figure supplement 1D**). As Akt is also a survival mediator this implicates that Nef-G63E mutation may be Th-cytopathic, decreasing Th dysfunctional expansion in LCMV (Recher et al., 2004) and HIV/SIV (Gray et al., 2011; Lindqvist et al., 2012; Petrovas et al., 2012) infections. Here, reduced peripheral $CXCR3^{-}CXCR5^{+}PD\text{-}1^{+}$ memory follicular Th (Tfh) (Locci et al., 2013) was in keeping (**Figure 4-figure supplement 1E** and **1F**).

We further explored molecular traits of this decreased Akt hyperactivation. We reasoned that comparing endogenous Nef binding patterns would be adequate and analyzed SIV-infected HSC-F cells with a flow cytometry-based proximity ligation assay (PLA) (Leuchowius et al., 2009; Avin et al., 2017), by calculating a mean fluorescence intensity (MFI) deviation-based binding index for each. We found that this Nef-G63E mutation causes significant decrease in Nef binding to PI3K p85/p110α and downstream mTORC2 components mTOR (Sarbassov et al., 2005) and GβL/mLST8 (Kim et al., 2003) in the $CD4^{lo}$-SIV Gag $p27^{+}$ infected population (**Figure 4D**). Collectively, the Nef-G63E mutation results in decreased aberrant Nef bridging and signal transduction of PI3K/mTORC2, explaining decreased substrate Akt Ser473 phosphorylation by mTORC2. Thus, Nef-G63E SIV is a mutant virus decreased in aberrant interaction/drive of B-cell-inhibitory PI3K/mTORC2 signaling. This molecular signature was reciprocal to a recently found human inborn error of immunity (IEI), activated PI3 kinase delta syndrome (APDS) (Angulo et al., 2013; Lucas et al., 2014; Avery et al., 2018).

Targeting of lymph node Env-specific B cells by Nef *in vivo*

Next, we analyzed *in vivo* targeting of virus-specific B cells by Nef in lymph nodes to explore the potential B-cell-intrinsic influence of the G63E-Nef phenotype. Previously suggested influence of soluble Nef itself (Qiao et al., 2006) and/or related host factors (Swingler et al., 2008) may derive generalized influence on B cells; however, SIV antigen-specific binding antibody responses were rather decreased in NAb inducers (**Figure 1-figure supplement 1**), viremia was comparable (**Figure 3-figure supplement 1C**) and ferritin levels were not altered (**Figure 4-figure supplement 1A**), arguing against these. Therefore, we surmised that some targeted Nef intrusion against Env-specific B cells may be occurring and that the decreased aberrant Nef-PI3K/mTORC2 drive may result in their enhanced lymph node maturation.

While reports (Xu et al., 2009) histologically proposed Nef B-cell transfer, quantitative traits, e.g., invasion frequency and influence on virus-specific B cells, have remained unvisited. Intracellular Nef staining is dim (particularly for B cell-acquired Nef), difficult to examine by conventional flow cytometry. Defining staining cutline requires single-cell images, overcoming confounding of high Nef false-staining via pre-permeation rupture and post-permeation confounding as judged by biologically discontinuous staining and/or batch-inflated signals. Collectively, at the expense of spatial information, we judged that sophisticating imaging cytometry would best visualize Nef-mediated B-cell perturbation *in vivo*. We analyzed lymph node B cells with Image Stream X MKII, with high-power (> 10-fold) antigen detection [e.g., molecules of equivalent soluble fluorochrome (MESF) 5 *vs.* MESF 80 in an average flow cytometer for FITC detection] ideal for detection/single-cell verification.

We designed a triple noise cancellation strategy to overcome the above. Firstly, amine reactive dye staining (Perfetto et al., 2006) gated out B cells being Nef-positive due to pre-experimental membrane damage (**Figure 5-figure supplement 1A**, left). Next, we deployed secondary quantitative parameters of Nef signals deriving from each pixel of the images. Definition of a gray-level cooccurrence matrix (GLCM) (Haralick et al., 1973) numerating

adjacent signal deviation as their frequencies on a transpose matrix enables calculation of a variety of feature values summarizing traits of the whole image. A biological assumption of Nef signal continuity in a true staining suggested that the sum of weighted square variance of GLCM, i.e., the {sum of [square of (value – average signal strength) × frequency of each value occurrence]} would separate natural versus artificial Nef signals. This value, Haralick variance, was computed for multiple directions and averaged, deriving Haralick variance mean (**Figure 5-figure supplement 1A**, X axis), proportionate with staining image unnaturalness. Finally, Nef signal intensity threshold (**Figure 5-figure supplement 1A**, Y axis) gated out overtly-stained cells void for true-false verification. These excluded B cells showing non-specific, strong-signal binary-clustered staining pixels for Nef deriving a large summated variance (X axis), and/or cells batch-stained for Nef (Y axis), likely originating from post-experimental membrane damage.

With this approach we acquired images of a Live/Dead^{-}-Nef signal Haralick variance mean^{lo}-Nef signal intensity threshold^{lo}-Nef^{+}CD19^{+} B-cells, with fine-textured gradation of Nef^{int-lo} staining with continuity from membrane-proximal regions without sporadic staining speckles (**Figure 5A** and **Figure 5-figure supplement 1A**). Images resembled Nef-transferred B cells generated *in vitro* by a SIV-infected CD4+ T-cell coculture (**Figure 5-figure supplement 1B**). A linear discriminant analysis-based machine learning module, scoring segregation of typical void/valid images, showed this gating to provide the highest two-dimensional separation (**Figure 5-figure supplement 1A**). Combined with biotinylated Env/streptavidin staining, this reproducibly obtained images of Env-specific (Ch 12) CD19^{+} (Ch 11) B cells without membrane ruptures (Ch 08) and showing fine-textured transferred Nef (Ch 02) (**Figure 5B**). Nef invasion upregulated pAkt Ser473 (Ch 03) to a range resembling *in vitro* analysis (**Figure 5C**), stating that Nef-driven aberrant PI3K/mTORC2 signaling does occur in Nef-invaded B cells *in vivo* and the current phenotypic change likely affects B-cell dynamics. Strikingly, lymph node Env-specific B cells showed significantly higher Nef-positive frequencies as compared with batch non-Env-specific B cells (**Figure 5D**). This indicated that infected cell-generated Nef preferentially targets adjacent Env-specific B cells, putatively through infected CD4^{+} cell-to-B-

cell contact/transfer (Xu et al., 2009; Hashimoto et al., 2016) and that a Nef phenotypic change likely dictates Env-specific B-cell maturation.

Enhanced Env-specific B-cell responses after PI3K-diminuting mutant selection

Finally, peripheral SIV Env-specific IgG$^+$ B-cell responses comprising plasmablasts (PBs) and memory B cells (B_{mem}) were analyzed to assess *in vivo* B-cell quality in NAb inducers with Nef-G63E mutant selection. After excluding lineage-specific cells [T/NK/pro-B cells/monocytes/myeloid dendritic cells (DCs)/plasmacytoid DCs], we defined IgG$^+$ PBs as showing: high replication (Ki-67$^+$), post-activation (HLA-DR$^+$), transcriptional switching for terminal differentiation (IRF4^{hi}) and downregulated antigen surface binding (surface [s]Env^{lo}-cytoplasmic [Cy]Env$^+$) (Nutt et al., 2015; Silveira et al, 2015). Env-specific PBs were defined as CD3$^-$CD8$^-$CD10$^-$CD14$^-$CD16$^-$CD11c$^-$CD123$^-$CD19$^-$CyIgG$^+$Ki-67$^+$IRF4^{hi}HLA-DR$^+$ (total PB) sEnv^{lo}CyEnv$^+$ (Env-specific) (**Figure 6-figure supplement 1**). NAb inducers showed significantly higher Env-specific IgG$^+$ PB responses around week 30 p.i., after Nef-G63E selection, compared to those in NAb non-inducers (**Figures 6A** and **6B**). At 1 year, this difference became enhanced; Env-specific PBs were reduced in non-inducers, while this reduction was ameliorated in the NAb inducers with Nef-G63E.

Concomitant determination of Env-specific IgD$^-$CD27$^+$IgG$^+$ B_{mem} responses allowed pair-wise analysis of Env-specific IgG$^+$ B_{mem}/PB as a projection of germinal center (GC) output as an indicator of overall B-cell response quality (Zotos et al., 2010) (**Figure 6C**, left). In this two-dimensional vector charting of Env-specific B_{mem}/PB responses, vector protrusion towards upper right reasonably represents higher gross GC output of antibody-forming cells (AFCs) (B_{mem}/PBs). In NAb non-inducers, all vectors converged on an empirically defined polygonal attractor area D_n (gray area surrounded with dotted lines in **Figure 6C**, right) at year 1 p.i. and beyond, describing that these NAb non-inducers failed to sustain Env-specific GC output. In contrast, the vectors were consistently tracked outside D_n in the NAb inducers with Nef G63E (**Figure 6C**). At the moment of NAb induction, they converged on another upper-right GC output attractor area D_i (red area surrounded with dotted lines in **Figure 6C**, right), mutually

exclusive with D_n (P < 0.0001 by Fisher's exact test on NAb non-inducer/inducer vector distribution frequency within D_n). These suggest more robust virus-specific IgG$^+$ B-cell responses following Nef-G63E CD8$^+$ T-cell escape mutant selection, predisposing to NAb induction. This enhanced cognate B-cell signature was also an inverted pattern of impaired terminally-differentiated B-cell responses in APDS (Al Qureshah et al., 2021).

Taken together, in the current model, Nef$_{62\text{-}70}$-specific CD8$^+$ T-cell responses in persistently SIV$_{mac239}$-infected macaques selected for an escape mutant, Nef-G63E SIV, which decreased aberrant Nef binding and drive of B-cell-inhibitory PI3K/mTORC2. B-cell Nef invasion *in vivo* occurred more preferentially in Env-specific B cells, suggesting diminution in tonic Nef-mediated B-cell dysregulation after mutant selection. These predisposed to enhanced Env-specific B-cell responses and subsequent SIV$_{mac239}$-specific NAb induction, altogether, in a manner reciprocal to human APDS-mediated immune dysregulation.

Discussion

In the present study, we found NAb induction against an NAb-resistant SIV after selection of a $CD8^+$ T-cell escape *nef* mutant virus. The Nef-G63E mutation, positioned in cognate B cells, results in reduction of binding/drive of PI3K/mTORC2, being concordant with *in vivo* enhancement of Env-specific IgG^+ B cells up to NAb induction following mutant selection. Importantly, this manifested through a pAkt deviation level more vivid than wild-type versus germline *PIK3CD* gain-of-function mutation heterozygote mice showing full APDS phenotype, stating that the current Nef-G63E-associated B-cell/NAb phenotype likely occurs in a “reciprocal APDS-like” manner. This proposition was enhanced based on extension of immune cell-intrinsic Nef influence on cognate B cells (Fig. 5), in addition to infected T cells. This work is, to our knowledge, the first to interlink a PI3K/mTORC2-modulating viral signature and enhanced B-cell/NAb responses in a viral infection model.

A link between viral T-cell escape and consequent immune modulation has been previously partially explored, including enhanced mutant HIV-1 epitope peptide binding to inhibitory MHC-I receptor on DCs impairing T cells (Lichterfeld et al., 2007) and decreased CTL-mediated lymph node immunopathology rather driving LCMV-specific antibody production (Battegay et al., 1993). Our results now evidence a new pattern of NAb responses bivalently shaped through viral interactions with both humoral and cellular immunity in AIDS virus infection. SIV_{mac239} infection of macaques possessing MHC-I alleles associated with Nef-G63E mutation can be one unique model to analyze virus-host interaction for B cell maturation leading to NAb induction. A *nef* polymorphism was extracted, partially appending to a virological impact of Nef (Kirchhoff et al., 1995; Gauduin et al., 2006; Stolp et al., 2012) in perturbing immunity whereas the current phenotype differed from such replication-related properties. The *nef* region encoding Nef-G63E is not conserved in HIV-1 (Schindler et al., 2004) and beyond this model study it remains to be addressed whether mutant HIV-1 with a similar phenotype can be obtained.

The major *in vivo* readout of this study is autologous neutralization of a highly resistant

SIV, differing from HIV-specific broadly neutralizing antibodies (bNAbs). Importantly, however, obtained signatures of enhanced IgG$^+$ Env-specific AFC B cells (class switch/terminal differentiation) and virus neutralization (hypermutation) directly evidence enhanced activity of activation-induced cytidine deaminase (AID), the canonical positive driver of B-cell fate, showing a strong conceptual continuity with bNAb regulation by AID.

Our results extracted an *in vivo* link between a decreased aberrant Nef-PI3K/mTORC2 interaction and major enhancement in B-cell responses. The relationship is indeed reciprocal to immunogenetic mechanisms of human PI3K gain-of-function mutations resulting in APDS with multiply impaired anti-viral B-cell responses. While the exact hierarchy of binding between Nef and PI3K/mTORC2 components (including PI3K isoforms) and its perturbation by Nef-G63E mutation remains much to be investigated, PI3Kp85 did reasonably show the strongest Nef-binding index in PLA assay (**Figure 4D**) as Nef and PI3Kp85 possess SH3-binding PxxP and SH3 domains, respectively (Rickles et al., 1994). Binding decrease in canonical partner PI3Kp85 may domino-trigger decrease with others, resulting in quadruple PI3K/mTORC2 binding decrease and fragile downstream Akt signaling.

In conclusion, we exemplify in a non-human primate AIDS model that NAb induction against a highly resistant SIV occurs after selection of a CD8$^+$ T-cell escape variant reduced in excess PI3K/mTORC2 drive. These results provide an understanding of how immunodeficiency virus-specific NAb responses can be shaped by both wings of adaptive immune pressure and depicts that immune cell-intrinsic PI3K/mTORC2 manipulation may be pivotal for harnessing antiviral NAb responses. Furthermore, search of other analogies between viral immune dysregulations and human IEIs may lead to identification of novel targets to modulate and harness immune responses in translational settings.

Limitations of study

A limitation of this study is the use of retrospective samples, posing constraints for detecting exact temporal changes in tonic viral B-cell perturbation. Related with this, sampling of lymph node cells in animals belonging to the subgroup of interest at the optimal moment was

unpredictable. Nevertheless, usage of such specific animal models does help to depict a temporal cascade of *in vivo* events leading to NAb induction, assisting human immunology. As future extension of this study extracting the NAb-involved molecular axis, manipulation/reconstitution experiments shall be designed.

Acknowledgments

This work was supported by Japanese Initiative for Progress of Research on Infectious Diseases for Global Epidemic (J-PRIDE) (JP19fm0208017 to H.Y.), Japan Program for Infectious Diseases Research and Infrastructure (Interdisciplinary Cutting-edge Research) (JP22wm0325006 to H.Y.), Research Programs on HIV/AIDS, Emerging and Re-emerging Infectious Diseases, and Global Health Issues (JP20fk0410022 to H.Y.; JP18fk0410003, JP20fk0410011, JP20fk0108125, JP20jm0110012, JP21fk0410035, and JP21jk0210002 to T.M.) from Japan Agency for Medical Research and Development, the Ministry of Education, Culture, Sports, Science, and Technology in Japan ([JSPS] KAKENHI Grants 17H02185 and 18K07157 to H.Y.; 21H02745 to T.M.), the Takeda Science Foundation (to H.Y.) and the Imai Memorial Trust for AIDS Research (to H.Y.). We thank Fumiko Ono, Koji Hanari, Katsuhiko Komatsuzaki, Akio Hiyaoka, Hiromi Ogawa, Keiko Oto, Hirofumi Akari, Yasuhiro Yasutomi, Hiromi Sakawaki, Tomoyuki Miura and Yoshio Koyanagi for animal experiment assistance; Hiroyuki Kogure, Sayuri Seki and Julia R. Hirsiger for imaging cytometry technical assistance; Masako Nishizawa, Trang Thi Thu Hau, Shigeyoshi Harada, Takushi Nomura, Akiko Takeda, Taku Nakane, Nami Iwamoto, Taeko K. Naruse, Akinori Kimura and Mark S. de Souza for their help. H.Y. thanks Jun Abe, Shoi Shi, Bettina Stolp, Jens V. Stein, Makoto Yamagishi and Yusuke Yanagi for conceptual discussions.

Author Contributions

H.Y. conceived/designed/performed study and wrote manuscript; T.M. provided animal cohort, co-edited manuscript and co-directed study.

Declaration of Interests

The authors declare no competing interests.

Figure Legends

Figure 1. NAb induction against NAb-resistant SIV_{mac239}.

(A) Study design.

(B) Plasma viral loads (SIV *gag* RNA copies/ml plasma) in NAb non-inducers (left) and inducers (right). Viral loads have been previously partially reported (Yamamoto et al., 2007; Nomura et al., 2012; Takahashi et al., 2013; Nakane et al., 2013; Iwamoto et al., 2014).

(C) Plasma SIV_{mac239} 100% neutralizing end point titers by 10 $TCID_{50}$ killing assay on MT4-R5 cells. Points on the dotted line show marginally NAb-positive results ($<$ 1:2). In some animals, titers were comparable with our reported results using MT4 cells (Kawada et al., 2007).

Figure 2. Selection of a viral *nef* mutation (Nef-G63E) before NAb induction.

(A) Viral *nef* mutations in NAb inducers. A linear schema indicating Nef functional domains is aligned above. Mutations at timepoints with NAb^- (indicated by white wedge; mostly before 6 months p.i.), $NAb^{+/-}$ (green wedge) and NAb^+) (purple wedge; mostly after 1 year) are shown in individual animals. Black and dark gray represent dominant and subdominant mutations (or deletion in R-360) by direct sequencing, respectively. Red and pink indicate dominant and subdominant G63E detection, respectively.

(B) Schema of SIV_{mac239} Nef structure and Nef-G63E mutation orientation.

(C) Comparison of frequencies of macaques having Nef-G63E in plasma viruses between NAb non-inducers and inducers. Compared by Fisher's exact test.

(D) Temporal relationship of Nef G63E frequencies in plasma virus and NAb induction. Black boxes (left Y axis) show log_2 NAb titers; red triangles and green diamonds (right Y axis) show percentage of G63E and G63R mutations detected by subcloning (15 clones/point on average), respectively.

Figure 3. Nef-G63E is a $CD8^+$ T-cell escape mutation.

(A) $Nef_{62–70}$ QW9-specific $CD8^+$ T-cell frequencies and related MHC-I alleles in seven NAb

inducers selecting Nef-G63E. Mamu-B*039:01 and Mamu-B*004:01 are known to restrict $Nef_{62–70}$ QW9 epitope (Evans et al., 1999; Sette et al., 2012) and binding of $Nef_{63–70}$ peptide to Mamu-A1*032:02 was predicted.

(B) $CD8^+$ T-cell responses specific to wild-type $Nef_{62–70}$ or mutant $Nef_{62–70}$.G63E or $Nef_{62–70}$.G63R peptides. See also Figure S3.

Figure 4. Nef-G63E mutation reduces PI3K/mTORC2 binding and pAkt drive.

(A) Representative surface expression level histograms of CD3, CD4, MHC class I, CXCR4 and BST-2 after wild-type (WT) or Nef-G63E mutant SIV infection at multiplicity of infection (MOI) 0.1 on HSC-F cells.

(B) Left: representative histograms of relative pAkt serine (Ser) 473 levels in $p27^+$ cells after WT or Nef-G63E mutant SIV infection at MOI 0.1 on HSC-F cells. Numbers show pAkt Ser473 mean fluorescence intensities (MFIs) for each. Right: Deviation of pAkt Ser473 MFIs in $p27^+$ HSC-F cells compared with mean MFI of uninfected cells. Compared by unpaired t test.

(C) Left: Relative pAkt Ser473 levels (normalized to mean MFI of uninfected controls) in Nef^+ HSC-F cells assessed for serum starvation (MOI 0.2, 1 day p.i.). Adjusted *P* values show results of comparison via Sidak's post-hoc test of 2-way ANOVA (C, left). Right: Deviation of pAkt Ser473 MFIs in Nef^+ HSC-F cells assessed for high-MOI infection (MOI 5, 1-day p.i.). Compared by unpaired t test.

(D) Proximity ligation assay (PLA) of Nef binding with mTOR, GβL/mLST8, PI3Kp85 and PI3Kp110α. MFI-based binding index was calculated as (anti-Nef/anti-partner) - (isotype/anti-partner) - (anti-Nef/isotype) + (isotype/isotype). Histograms for samples and isotype/isotype are representatively shown. Differences in MFI binding indexes can be enhanced compared with comparison of raw MFIs. Compared by paired t tests. Data represent one of two [(A); (B); (C, right)] independent experiments in quadruplicate, four independent experiments performed in triplicate [(C, left)] or four independent single-well comparison experiments pooled for statistical analysis (D). Bars: mean ± SD (B, C right), mean ± SEM (C left).

Figure 5. Preferential targeting of lymph node Env-specific B cells by Nef *in vivo*.

(A) Representative gating of triple noise-cancellation *in vivo* Nef staining in B cells analyzed by ImageStreamX MKII. Pre-experimental damaged cells are first excluded with Live/Dead from focused/centroid/singlet image-acquired $CD19^+$ B cells (first lane right/R4 gated on "Focused"). Following Nef^+ gating (second lane left/R5 gated on R4), a second step of Nef noise cancellation (second lane middle/R7 on R5) comprises double-negative removal of post-experimental stochastic irregular staining building a disparate intracellular staining gradient (X axis, Nef signal pixel Haralick variance mean) and post-experimental batch overt cellular staining (Y axis, Nef signal pixel intensity threshold). This outputs a B-cell population with a fine-textured pericellular $Nef^{int\text{-}lo}$ staining, biologically concordant with Nef membrane-anchoring. Probing of anti-Env BCR (αEnv) by recombinant SIV Env (second lane, right) is combined, resulting in a 2-D panel of intracellular Nef versus αEnv for noise-cancelled Nef^+ B cells (R7) plus Nef^- B cells (R8) (third lane left/"R7+R8"). pAkt Ser473 expression (third lane right) and cellular morphology (B) was further analyzed.

(B) Typical images of Nef-transferred Env-specific B cells defined αEnv^+-intracellular Nef^+-Nef Haralick variance $mean^{lo}$-Nef Intensity $threshold^{lo}$-$Live/Dead^-$-$CD19^+$ cells ["Nef^+aEnv^+" population of lower left panel in (A), gated on "R7, R8"]. Note the pericellular pAkt Ser473 upregulation in these cells (Ch 03/yellow). Data on inguinal lymph node lymphocytes of macaque R10-007 at week 62 post-SIV_{mac239} infection are shown in (A) and (B).

(C) Comparison of pAkt Ser473 median fluorescence (medFI) intensity levels in Nef^- B cells (R8) versus noise-cancelled Nef^+ B cells (R7). Analyzed by paired t test.

(D) Comparison of Nef-positive cell frequencies in non-Env-specific (left) versus Env-specific (right) B cells in lymph nodes of persistently SIV-infected macaques (n = 6). Analyzed by paired t test.

Figure 6. Enhanced SIV Env-specific B-cell output up to NAb induction following Nef-G63E selection.

(A) Changes in SIV Env gp140-specific plasmablast (PB) frequencies in viremic NAb non-

inducers (left, n = 12) and Nef-G63E-selecting NAb inducers (right, n = 6). Available samples of twelve viremic NAb non-inducers (including ten with ≥ 1-year survival) and six NAb inducers were tracked. In the right panel, the frequencies in NAb non-inducers are shown in background (gray) for comparison.

(B) Comparison of Env gp140-specific PB frequencies between NAb non-inducers and inducers by Mann Whitney U tests. In the right, the frequencies at NAb induction were compared with those at year 1 in NAb non-inducers with ≥ 1-year survival (n = 10). Bars: mean ± SD.

(C) Left: vector chart of Env gp140-specific memory B cell (B_{mem}) and PB levels. Legends for each animal correspond to the ones in (B). Right: NAb non-inducer vectors empirically define a polygonal GC output attractor area D_n (gray area surrounded with dotted lines) on which they converge by and beyond year 1 p.i. The NAb inducer vectors (shown up to the time of NAb induction) remained outside of D_n. At the moment of NAb induction they converged on a second GC output attractor area D_i (red area surrounded with dotted lines), mutually exclusive with D_n (P < 0.0001 by Fisher's exact test on NAb inducer vector convergence frequency within D_n). Legends for year 1 p.i. in the NAb non-inducers and moment of NAb induction in the NAb inducers are specified.

Materials and Methods

Material availability

This study did not generate new unique reagents.

Data and code availability

Data were analyzed using existing computational packages. The accession number for the transcriptome data [wild-type SIV_{mac239}-infected HSC-F cell line (*n* = 3), Nef-G63E SIV_{mac239}-infected HSC-F cell line (*n* = 3) and uninfected HSC-F cell line (*n* = 3)] has been deposited under the accession number GenBank: GSE65806.

Rhesus macaques retrospectively utilized for samples

Seventy Burmese rhesus macaques (*macaca mulatta*) (57 males and 13 females) were retrospectively analyzed in this study. Experiments were previously carried out (Matano et al., 2004; Yamamoto et al., 2007; Iseda et al., 2016; Nomura et al., 2012; Ishii et al., 2012; Takahashi et al., 2013; Nakane et al., 2013; Shi et al., 2013; Iwamoto et al., 2014; Terahara et al., 2014) in the Tsukuba Primate Research Center, National Institutes of Biomedical Innovation, Health and Nutrition (NIBIOHN) with the help of the Corporation for Production and Research of Laboratory Primates and the Institute for Frontier Life and Medical Sciences, Kyoto University (IFLMS-KU) after approval by the Committee on the Ethics of Animal Experiments of NIBIOHN and IFLMS-KU under the guidelines for animal experiments at NIBIOHN, IFLMS-KU and National Institute of Infectious Diseases in accordance with the Guidelines for Proper Conduct of Animal Experiments established by Science Council of Japan (http://www.scj.go.jp/ja/info/kohyo/pdf/kohyo-20-k16-2e.pdf). The experiments were in accordance with the "Weatherall report for the use of non-human primates in research" recommendations (https://royalsociety.org/topics-policy/publications/2006/weatherall-report/). Animals were housed in adjoining individual primate cages allowing them to make sight and sound contact with one another for social interactions, where the temperature was kept at

523 25°C with light for 12 hours per day. Animals were fed with apples and commercial monkey
524 diet (Type CMK-2, Clea Japan, Inc.). Blood collection and virus challenge were performed
525 under ketamine anesthesia.
526
527 **Cells and viruses**
528 MT4-R5 cells were maintained in RPMI1640 (Invitrogen) supplemented with 10% fetal bovine
529 serum (FBS) (Clontech) and antibiotics. HSC-F cells (cynomolgus $CD4^+$ T-cell line) and
530 HSR5.4 cells (rhesus macaque $CD4^+$ T-cell line) were maintained in RPMI1640 (Invitrogen)
531 supplemented with 10% fetal bovine serum (FBS) (Clontech), human interleukin-2 (IL-2) (10
532 IU/ml, Roche), 4-(2-hydroxyethyl)-1-piperazineethanesulfonic acid (HEPES) (Invitrogen) and
533 2-mercaptoethanol (Gibco). Rhesus macaque primary $CD20^+$ B cells were magnetically
534 isolated from peripheral blood mononuclear cells (PBMCs) with anti-CD20 microbeads
535 (Miltenyi Biotec). SIV_{mac239} molecular clone derivative was generated by mutagenesis PCR
536 (Agilent Technologies) using the primers listed. For virus preparation, COS-1 cells were
537 transfected with pBR_{mac239} proviral DNA using FuGENE 6 (Promega). At 48 h post-transfection,
538 culture supernatants were harvested, centrifuged and filtered through a 0.45-μm pore-size
539 filter (Merck Millipore). To titrate infectivity, prepared viruses were serially diluted and infected
540 on HSC-F cells in 96-well plates (Falcon) in quadruplicate. At 10 days post-infection, the
541 endpoint was determined using SIV p27 antigen enzyme-linked immunosorbent assay
542 (ELISA) kit (ABL), and virus infectivity was calculated as the 50 percent tissue culture infective
543 dose ($TCID_{50}$) according to the Reed-Muench method.
544
545 **Identification of SIV_{mac239}-NAb inducers**
546 Burmese rhesus macaques previously challenged with the highly pathogenic molecular clone
547 virus SIV_{mac239} (n = 70) were retrospectively examined approximately up to 2 years for their
548 plasma NAb profiles. Animals were challenged intravenously with 1,000 $TCID_{50}$ of SIV_{mac239}.
549 In the current study, virological and immunological profiles were compared between the newly
550 identified NAb inducers (n = 9) and representative NAb non-inducers (n = 19). These NAb

551 non-inducers and eight NAb inducers except R06-032 were previously partially reported for
552 their plasma viral loads (Yamamoto et al., 2007; Iseda et al., 2016; Nomura et al., 2012;
553 Takahashi et al., 2013; Nakane et al., 2013; Iwamoto et al., 2014) (**Figure 1B**). MHC-I
554 haplotypes and alleles were determined by reference strand-mediated conformation analysis,
555 PCR-SSP (PCR amplification utilizing sequence-specific priming) and cloning as described
556 (Naruse et al., 2010). MHC-I binding prediction was made on April 27, 2013 using the IEDB
557 analysis resource NetMHCpan tool (Hoof et al., 2009). Alleles of interest in the study have
558 been previously identified in macaques (Nomura et al., 2012; Evans et al., 1999; Sette et al.,
559 2012). Macaques R06-032, R03-015, R01-010 and R05-010 received a prime-boost
560 vaccination (Matano et al., 2004) composed of a DNA prime/intranasal Sendai virus vector
561 expressing SIV_{mac239} Gag (SeV-Gag). R03-015, R06-019, R06-038 and R10-001 received 300
562 mg of non-specific rhesus IgG at day 7 post-SIV_{mac239} challenge as an experimental control in
563 our previous reports (Yamamoto et al., 2007; Iseda et al., 2016; Nakane et al., 2013).
564
565 **Plasma viral load quantitation**
566 Plasma viral RNA samples were extracted with High Pure Viral RNA kit (Roche Diagnostics).
567 Serial fivefold sample dilutions were amplified in quadruplicate by reverse transcription and
568 nested PCR using SIV_{mac239} *gag*-specific primers to determine end point via the Reed-Muench
569 method as described previously (Matano et al., 2004; Iseda et al., 2016). The lower limit of
570 detection is approximately 400 viral RNA copies/ml plasma.
571
572 **SIV_{mac239}-specific neutralization assay**
573 NAbs were titrated as described (Yamamoto et al., 2007; Iseda et al., 2016). Serial twofold
574 dilutions of heat-inactivated plasma, or polyclonal IgG affinity-purified with Protein G
575 Sepharose 4 Fast Flow (GE Healthcare) from heat-inactivated and filtered plasma were mixed
576 with 10 $TCID_{50}$ of SIV_{mac239} at a 1:1 ratio (5 μl:5 μl) in quadruplicate. After 45-min incubation at
577 room temperature, the 10 μl mixtures were added into 5 x 10^4 MT4-R5 cells/well in 96-well
578 plates. Progeny virus production in day 12 culture supernatants was examined by SIV p27

579 ELISA (ABL) to determine 100% neutralizing endpoint. The lower limit of titration is 1:2.
580 Neutralization in three out of four wells at a dilution of 1:2 is defined as marginally NAb-positive
581 (< 1:2). Results were comparable when the same assay was performed with macaque HSC-
582 F cells (Akari et al., 1996) as targets. NAb inducers R01-012, R02-004, R01-010, R02-007
583 and NAb non-inducer R01-011 were previously partially reported for their NAb titers measured
584 with the same method using MT4 cells as targets (Kawada et al., 2007), which derived
585 comparable results. For assessment of neutralizing activity in IgG, SIV_{mac239}-specific IgGs
586 purified from pools of plasma with SIV_{mac239}-specific NAb titers were obtained from each animal
587 as described (Yamamoto et al., 2007). After complement heat-inactivation at 56°C, 30 min and
588 0.45 μm filtration, IgGs were purified by Protein G Sepharose 4 Fast Flow (GE Healthcare)
589 and concentrated by Amicon Ultra 4, MW 50,000 (Millipore) to 30 mg/ml and similarly
590 examined for their 10 $TCID_{50}$ SIV_{mac239} killing titers on MT4-R5 cells.
591
592 **SIV Env-specific IgG ELISA and immunoblotting**
593 Plasma Env-specific IgG titers were measured as described (Nakane et al., 2013). SIV_{mac251}
594 Env gp120 (ImmunoDiagnostics) were coated on 96-well assay plates (BD) at 1000 ng/ml
595 (100 μl/well). Wells were prewashed with phosphate-buffered saline (PBS), blocked with 0.5%
596 bovine serum albumin (BSA)/PBS overnight and plasma samples were incubated at a 1:20
597 dilution (5 μl:95 μl) for 2 hours. Wells were washed with PBS and SIV Env-bound antibodies
598 were detected with a horseradish peroxidase (HRP)-conjugated goat anti-monkey IgG (H+L)
599 (Bethyl Laboratory) and SureBlue TMB 1-Component Microwell Peroxidase Substrate (KPL).
600 Absorbance at 450 nm was measured. Samples from week 0 pre-challenge and month 3,
601 month 6 and year 1 post-challenge were assessed in duplicate. Week 0 average values were
602 subtracted from corresponding later time point values for calibration. For immunoblotting, SIV
603 virion-specific IgGs in plasma were detected with a SIV_{mac239}-cross-reactive western blotting
604 system (ZeptoMetrix). In the NAb non-inducers, samples from those showing rapid
605 progression (euthanized due to AIDS progression within approximately 1 year) with low

plasma anti-SIV reactivity (Nakane et al., 2013) were not included.

Sequencing

Sequencing was performed as described (Matano et al., 2004; Iseda et al., 2016). Viral cDNA fragments spanning from nt (nucleotide) 4829 to nt 7000, nt 6843 to nt 8831 and nt 8677 to nt 10196 in SIV_{mac239} (GenBank accession number MM33262) covering SIV *env* and *nef* were amplified from plasma viral RNA by nested RT-PCR using Prime-Script one-step RT-PCR kit v2 (TaKaRa) and KOD-Plus v2 (Toyobo). PCR products were either directly sequenced or subcloned with a TOPO blunt-end cloning system (Invitrogen). Sequencing was performed using dye terminator chemistry with an ABI 3730 DNA sequencer (Applied Biosystems). On average, 15 clones were obtained per sample and 20 clones were assessed when *nef* mutations of interest in early time points were subdominant.

SIV_{mac239}-specific $CD8^+$ T-cell responses

Virus-specific $CD8^+$ T-cell frequencies were measured as described (Matano et al., 2004; Iseda et al., 2016). Peripheral blood mononuclear cells (PBMCs) were cocultured for 6 hours with autologous herpesvirus papio-immortalized B lymphoblastoid cell lines (B-LCLs) pulsed with Nef peptides (Sigma-Aldrich Japan) at 1 μM concentration or as indicated otherwise under GolgiStop (monensin, BD) presence. Intracellular gamma interferon (IFN-γ) staining was performed using Cytofix/Cytoperm kit (BD) and the following conjugated anti-human monoclonal antibodies (mAbs): anti-CD4-FITC (M-T477, BD Pharmingen), anti-CD8-PerCP (SK1, BD Biosciences), anti-CD3-APC (SP34-2, BD Pharmingen) and anti-IFN-γ-PE (4S.B3, BioLegend). Specific $CD8^+$ T-cell frequencies were determined by subtracting nonspecific IFN-γ^+ $CD8^+$ T-cell frequencies from those after peptide-specific stimulation; frequencies beneath 100 cells/million PBMCs were considered negative. Cells acquired by FACS Canto II (BD) were analyzed by FACS Diva (BD) and FlowJo (Treestar). Approximately 1 x 10^5 PBMCs were gated per test.

Nef-mediated signaling perturbation analysis

Virus supernatants obtained from COS-1 cells after transfection with wild-type or mutant SIV_{mac239} molecular clones were used for infection of $CD4^+$ T-cell lines, cynomolgus macaque-derived HSC-F and rhesus macaque-derived HSR5.4 (Akari et al., 1996). QuikChange II XL site-directed mutagenesis kit (Agilent Technologies) was used to construct a mutant SIV_{mac239} molecular clones possessing a *nef* mutation Nef G63E (G-to-A mutation at nt 9520) from the wild-type SIV_{mac239} molecular clone (Kestler et al., 1991) (nt number from GenBank accession number M33262). Cells (1 x 10^5 cells/well in U-bottomed 96-well culture plates [BD]) were infected with wild-type or mutant SIV_{mac239} cultured in RPMI-1640 medium supplemented with 10% fetal bovine serum (FBS) for indicated periods at MOI 0.1 (intracellular signaling analysis) or 0.001 (supernatant analysis). Culture supernatants were subjected to measurement of SIV capsid p27 concentrations by ELISA. Harvested cells were fixed and permeabilized with Cytofix/Cytoperm kit, washed twice and subjected to immunostaining. The following antibodies were used; anti-SIV_{mac251} Gag p27 mAb (ABL) manually conjugated with Alexa 647 (Life Technologies), anti-SIV_{mac251} Nef mAb (clone 17, epitope peptide corresponding to SIV_{mac239} Nef 71-80 not including the residue G63: Thermo Scientific/Pierce) manually conjugated with Alexa 647, anti-human CD3-APC-Cy7 (SP34-2, BD Pharmingen), anti-human CD4-PerCP (L200, BD Pharmingen), anti-human HLA-ABC-FITC (G46-2.6, BD Pharmingen), anti-human CXCR4-APC (12G5, BioLegend), BST2-Alexa647 (RS38E, BioLegend), Alexa 488-conjugated anti-phospho-Akt (Ser473) (D9E, CST) and Alexa 488-conjugated anti-phospho-Akt (Thr308) (C31E5E, CST). Cells acquired by FACS Canto II were analyzed by FACS Diva and FlowJo. Approximately 5 x 10^4 cells were gated for each test.

Ferritin ELISA

Plasma ferritin levels in NAb inducers and control animals were analyzed by monkey ferritin sandwich ELISA kit (LS Bio) according to the manufacturer's instructions.

661 **PI3K stimulation assay**

662 5 x 10^4 HSC-F cells were infected with wild-type or Nef G63E mutant SIV_{mac239} at MOI 0.2 and
663 cultured for 1 day in medium supplemented with 10% (normal), 1% (1/10 starvation) or 0.1%
664 (1/100 starvation) FBS. For ligand stimulation (**Figure S4B**), cells at the end of 1-day culture
665 were pulsed for 20 minutes with 40 ng/ml of recombinant human IFN-γ (Gibco/Thermo Fisher),
666 100 IU/ml of recombinant human IL-2 (Roche Diagnostics) or 10 μg/ml of SIV_{mac251} Env gp130
667 (ImmunoDx). Cells were intracellularly stained using Cytofix/Cytoperm kit with anti-SIV_{mac251}
668 Nef mAb or anti-SIV_{mac251} p27 mAb manually conjugated to Alexa 647 and PE-conjugated anti-
669 human phospho-Akt (Ser473) (D9E, CST) or Alexa 488-conjugated anti-human phospho-Akt
670 (Ser473). Cells acquired by FACS Canto II were analyzed by FACS Diva and FlowJo.
671 Approximately 7 x 10^4 HSC-F cells were gated per test.

672

673 **Transcriptome analysis**

674 Total RNAs were extracted using RNeasy Plus Mini kit (Qiagen) from 2 x 10^6 HSC-F cells 1
675 day after infection with wild-type or Nef G63E mutant SIV_{mac239} at MOI 5. Negative control RNA
676 samples were extracted from 2 x 10^6 uninfected HSC-F cells after culture with the same
677 condition. Three sets of experiments were performed. Total RNA samples were subjected to a
678 quality control (QC) analysis using an Agilent 2100 Bioanalyzer. The obtained amounts of total
679 RNAs were: 12.37 ± 0.39 (uninfected), 8.80 ± 0.44 (wild-type) and 9.02 ± 0.17 (Nef G63E) μg
680 (P = 0.66 for wild-type versus Nef G63E by unpaired t test). In all samples, two bands of 18S
681 and 28S rRNA were confirmed and the RNA integrity number (RIN) was 10. 500 ng of total
682 RNA samples were processed with GeneChip WT Plus reagent (Affymetrix/Thermo Fisher
683 Scientific) to produce 150 μl of fragmented and labeled cDNA samples. These were incubated
684 with a Human Gene 2.0 ST Array (Affymetrix/Thermo Fisher Scientific) for 16 hours, 60 rpm
685 at 45°C using GeneChip hybridization oven 645 (Affymetrix/Thermo Fisher Scientific). Results
686 were scanned with GeneChip Scanner 3000 7G (Affymetrix/Thermo Fisher Scientific) and
687 processed with Affymetrix Expression Console Software (Affymetrix/Thermo Fisher Scientific)

688 according to the manufacturer's instructions. Expression values were normalized by the RMA
689 method. Genes above mean background expression within the cognate sample and showing
690 significant difference between wild-type and Nef G63E SIV ($P < 0.05$ via unpaired t test for
691 $\log_2$-transformed values, 768 candidates) were determined. Akt-related genes exhibiting a
692 change of approximately 10% or more were representatively extracted and manually aligned
693 by the authors.
694
695 **Peripheral CD4$^+$ T-cell surface staining**
696 Cryopreserved/thawed PBMCs were stained for 30 minutes at 4°C with the following reagents
697 or conjugated anti-human mAbs: Live/Dead Aqua (Life Technologies), anti-CD4-PerCP (L200,
698 BD Pharmingen), anti-CD8-APC-Cy7 (RPA-T8, BD Pharmingen), anti-CD3-Alexa 700 (SP34-
699 2, BD Pharmingen), anti-CD95-PE-Cy7 (DX2, eBioscience), anti-CXCR5-PE (87.1,
700 eBioscience), anti-PD-1-Brilliant Violet 421 (EH12.2H7, BioLegend) and anti-CXCR3-Alexa
701 488 (G025H7, BioLegend). Cells acquired by FACS LSRII Fortessa (BD) were analyzed by
702 FACS Diva and FlowJo. Approximately 1.5 x 10^5 PBMCs were gated per test.
703
704 **Proximity ligation assay (PLA)**
705 A flow cytometry-based arrangement of proximity ligation assay (PLA) (Avin et al., 2017) was
706 performed to quantitatively assess Nef binding to candidate interacting molecules. 1 x 10^5
707 HSC-F cells were infected with SIV_{mac239} at MOI 0.05 in U-bottomed plates and permeated
708 with Cytofix/Perm kit (BD Biosciences). After two washes, they were resuspended in 0.5%
709 BSA/PBS for prevention of experimental procedure-related loss and stained with mouse anti-
710 SIV_{mac251} Nef mAb (clone 17, Thermo Scientific/Pierce) or mouse IgG1 isotype control mAb
711 (P3.6.2.8.1, Abcam) in combination with either of the following rabbit antibodies: anti-GβL
712 (86B8, CST), anti-mTOR (7C10, CST), polyclonal anti-human PI3K p85 (Merck Millipore), anti-
713 PI3 Kinase p110α (C73F8, CST) or rabbit IgG1 isotype control mAb (DA1E, CST). Antibody-
714 stained cells were subsequently probed with Duolink In Situ PLA Probe anti-mouse PLUS and
715 anti-mouse MINUS probes (Sigma/Merck). Next, they were detected for intermolecular binding

using Duolink flow PLA detection kit (Green) (Sigma/Merck) with a reaction time of 100 minutes for post-mouse/rabbit probe linking amplification. Finally, these PLA-subjected cells were additionally stained with anti-SIV_{mac251} Gag p27 mAb manually conjugated with Alexa 647 and anti-CD4-PerCP for 30 minutes for 20 minutes at 4°C. Cells acquired by FACS Canto II were analyzed by FACS Diva and FlowJo. Approximately 1 x 10^5 cells were gated per test. Binding index (Y axis) was calculated by deriving the deviation from the summation of: {baseline P: (MFI of background reaction with mouse isotype control/rabbit isotype control) + anti-Nef antibody-derived background Q: [(MFI of reaction with mouse anti-Nef/rabbit isotype control) - (MFI of background reaction with mouse isotype control/rabbit isotype control)] + anti-binding partner antibody-derived background R:[(MFI of reaction with mouse isotype control/rabbit anti-binding partner molecule) - (MFI of background reaction with mouse isotype control/rabbit isotype control)]}.

B-cell Nef invasion *in vitro* assay

For Nef invasion inhibition assay, 5 x 10^4 HSC-F cells were infected at MOI 1 for 48 hours. These were then additionally cocultured with 7.5 x 10^4 Ramos B cells for 12 hours. Ramos B cells were double-stained with Alexa 488-cojugated Nef and anti-CD19-PC-5.5 (J3-119, Beckman Coulter), and interacting infected cell-invaded B cell doublet images acquired with ImageStream X MKII (Amnis/Merck Millipore) were analyzed by IDEAS 6.3 (Amnis/Merck Millipore/Luminex).

Quantitative *in vivo* imaging flow cytometry

Cryopreserved/thawed lymph node cells (LNCs) from several persistently SIV-infected macaques used in previous experiments (Nakane et al., 2013; Takahashi et al., 2013; Iwamoto et al., 2014) were seeded in V-bottomed 96-well plates (Nunc) and blocked with 25 μg/ml of anti-human CD4 (clone L200: BD) in 100 μl volume for 15 minutes at 4°C. After three washes, they were stained with 10 μg/ml of recombinant SIV_{mac239} Env gp140-biotin (Immune

743 Technology) for 30 minutes at 4°C. Cells were then stained with anti-CD19-PC5.5 (J3-119,
744 Beckman Coulter), Live/Dead Aqua (Invitrogen) and streptavidin-APC-Cy7 (BioLegend) for 30
745 minutes at 4°C. After two washes, cells were processed with Cytofix/Cytoperm kit (BD) for 20
746 minutes at 4°C, washed twice, and next intracellularly stained with PE-conjugated anti-human
747 phospho-Akt (Ser473) (D9E, CST) and anti-SIV_{mac251} Nef mAb (clone 17, Thermo
748 Scientific/Pierce) manually conjugated with Alexa 488 or mouse IgG1 isotype control mAb
749 (P3.6.2.8.1, Abcam) for 30 minutes at 4°C. After final two washes, cells were suspended in
750 0.8% PFA/PBS. All centrifugations for washing (1,200 x g, 2 minutes) were performed at 4°C.
751 Cells were subjected to image acquisition with Image Stream X MKII imaging flow cytometer
752 (Amnis/Merck Millipore/Luminex) and analyzed with IDEAS 6.3 software (Amnis/Merck
753 Millipore/Luminex). Approximately 5 x 10^5 LNCs were acquired for analyses (**Figure 5**). A
754 custom-implemented linear discriminant analysis-based machine learning module (Luminex)
755 was utilized for verifying candidate Nef staining signal-related secondary parameters (**Figures**
756 **5** and **S5**) for their efficacy of target population separation.
757
758 **Peripheral SIV Env-specific B-cell responses**
759 Peripheral SIV Env gp140-specific memory B cells (B_{mem}) and plasmablasts (PBs) were
760 measured by flow cytometry with procedures modified from previous reports and our
761 experience (Silveira et al., 2015; Hau et al., 2022). First, cryopreserved/thawed PBMCs
762 seeded in V-bottomed 96-well plates (Nunc) were blocked with 25 μg/ml of anti-human CD4
763 (clone L200: BD) in 100 μl volume for 15 minutes at 4°C. This concentration attains blockade
764 of promiscuous SIV Env binding to CD4 comparable to levels by magnetic depletion of $CD3^+$
765 T cells (data not shown). After three washes, they were next stained with 10 μg/ml of
766 recombinant SIV_{mac239} Env gp140-biotin (Immune Technology) for 30 minutes at 4°C. They
767 were subsequently stained with the following anti-human antibodies and fluorochromes for 30
768 minutes at 4°C with combinations as follows; PB/B_{mem}: anti-CD3-APC-Cy7 (SP34-2, BD
769 Pharmingen), anti-CD8-APC-Cy7 (RPA-T8, BD Pharmingen), anti-CD14-APC-Cy7 (M5E2,

BioLegend), anti-CD16-APC-Cy7 (3G8, BioLegend), streptavidin-Brilliant Violet 421 (BioLegend), anti-CD19-PC5.5 (J3-119, Beckman Coulter) and Live/Dead Aqua (Invitrogen); PB: anti-CD10-APC-Cy7 (HI10a, BioLegend), anti-CD11c-PE-Cy7 (3.9, BioLegend), anti-CD123-PE-Cy7 (6H6, BioLegend) and anti-HLA-DR-PE-Texas Red (TU36, Invitrogen); B_{mem}: anti-CD27-PE/Dazzle 594 (M-T271, BioLegend), anti-CD10-PE-Cy7 (HI10a, BioLegend), anti-IgD-FITC (DaKo), anti-CD38-Alexa 647 (AT1, Santa Cruz Biotechnology), anti-IgG-Alexa 700 (G18-145, BD Pharmingen) and anti-CD138-PE (DL-101, eBioscience). After two washes, B_{mem} samples were suspended in 0.8% PFA/PBS. For PB staining, surface-stained cells were further processed with Cytofix/Cytoperm kit (BD) for 20 minutes at 4°C, washed twice, and next intracellularly stained with 10 μg/ml of recombinant SIV_{mac239} Env gp140-biotin (Immune Technology) for 30 minutes at 4°C. After three washes, they were next stained with anti-human IgG-PE (G18-145, BD), anti-human/mouse IRF4-eFluor 660 (3E4, eBioscience), anti-human Ki67-Alexa 700 (B56, BD Pharmingen) and streptavidin-Alexa 488 (BioLegend) for 30 minutes at 4°C. After final two washes, cells were suspended in 0.8% PFA/PBS. Cells acquired with FACS LSRII Fortessa were analyzed with FACS Diva and FlowJo. Approximately 1.5 x 10^5 PBMCs were acquired for B_{mem} and 4 x 10^5 PBMCs were acquired for PB analyses (**Figure 6**). All centrifugations for washing (1,200 x g, 2 minutes) were performed at 4°C. Env-specific PB frequencies were 0 cells/million PBMCs for pre-challenge samples in all animals examined, ruling out background confounding for high-sensitivity quantitation of the population.

Statistical Analysis

Analyses were performed via Prism 8 (GraphPad Software). $P < 0.05$ were considered significant in two-tailed unpaired t tests, paired t tests, Mann Whitney U tests, Fisher's exact tests, Wilcoxon signed-rank tests and two-way ANOVA with Sidak's post-hoc multiple comparison tests. For analysis of Nef-invaded B-cell pAkt levels, median fluorescence intensities (mFIs) were analyzed due to relatively small numbers of Nef^+ B cells. Analyses involving pAkt Ser473 levels all derived comparable results between mFI and MFI for wild type

versus Nef G63E virus. Machine learning-based rating of Nef signal parameters was verified with IDEAS 6.3 Machine Learning Module (Luminex).

References

Akari, H., Mori, K., Terao, K., Otani, I., Fukasawa, M., Mukai, R., and Yoshikawa, Y. (1996). In vitro immortalization of Old World monkey T lymphocytes with Herpesvirus saimiri: its susceptibility to infection with simian immunodeficiency viruses. *Virology* 218, 382–388.

Al Qureshah, F., Sagadiev, S., Thouvenel, C.D., Liu, S., Hua, Z., Hou, B., Acharya, M., James, R.G., and Rawlings, D.J. (2021). Activated PI3Kδ signals compromise plasma cell survival via limiting autophagy and increasing ER stress. *J Exp Med.* 218, e20211035.

Angulo, I., Vadas, O., Garçon, F., Banham-Hall, E., Plagnol, V., Leahy, T.R., Baxendale, H., Coulter, T., Curtis, J., Wu, C., et al. (2013). Phosphoinositide 3-kinase δ gene mutation predisposes to respiratory infection and airway damage. *Science* 342, 866–871.

Avery DT, Kane A, Nguyen T, Lau A, Nguyen A, Lenthall H, Payne K, Shi W, Brigden H, French E, et al. (2018). Germline-activating mutations in PIK3CD compromise B cell development and function. *J Exp Med* 215, 2073–2095.

Avin, A., Levy, M., Porat, Z., and Abramson, J. (2017) Quantitative analysis of protein-protein interactions and post-translational modifications in rare immune populations. *Nat. Commun.* 8, 1524.

Battegay, M., Moskophidis, D., Waldner, H., Bründler, M.A., Fung-Leung, W.P., Mak, T.W., Hengartner, H., and Zinkernagel, R.M. (1993). Impairment and delay of neutralizing antiviral antibody responses by virus-specific cytotoxic T cells. *J. Immunol.* 151, 5408–5415.

Baumjohann, D., Preite, S., Reboldi, A., Ronchi, F., Ansel, K.M., Lanzavecchia, A., and Sallusto, F. (2013). Persistent antigen and germinal center B cells sustain T follicular helper cell responses and phenotype. *Immunity* 38, 596–605.

Bradley, T., Peppa, D., Pedroza-Pacheco, I., Li, D., Cain, D.W., Henao, R., Venkat, V., Hora, B., Chen, Y., Vandergrift, N.A., et al. (2018). RAB11FIP5 Expression and Altered Natural Killer Cell Function Are Associated with Induction of HIV Broadly Neutralizing Antibody Responses. *Cell* 175, 387–399.e17.

Burns, D.P., Collignon, C., and Desrosiers, R.C. (1993). Simian immunodeficiency virus mutants resistant to serum neutralization arise during persistent infection of rhesus monkeys. *J. Virol.* 67, 4104–4113.

Cubas, R.A., Mudd, J.C., Savoye, A.L., Perreau, M., van Grevenynghe, J., Metcalf, T., Connick, E., Meditz, A., Freeman, G.J., Abesada-Terk, G. Jr., et al. (2013). Inadequate T follicular cell help impairs B cell immunity during HIV infection. *Nat. Med.* 19, 494–499.

Evans, D.T., O'Connor, D.H., Jing, P., Dzuris, J.L., Sidney, J., da Silva, J., Allen, T.M., Horton, H., Venham, J.E., Rudersdorf, R.A., et al. (1999). Virus-specific cytotoxic T-lymphocyte responses select for amino-acid variation in simian immunodeficiency virus Env and Nef. *Nat. Med.* 5, 1270–1276.

Fallet, B., Narr, K., Ertuna, Y.I., Remy, M., Sommerstein, R., Cornille, K., Kreutzfeldt, M., Page, N., Zimmer, G., Geier, F., et al. (2016). Interferon-driven deletion of antiviral B cells at the onset of chronic infection. *Sci. Immunol.* 1, pii: eaah6817.

François, F., and Klotman, M.E. (2003). Phosphatidylinositol 3-kinase regulates human immunodeficiency virus type 1 replication following viral entry in primary CD4+ T lymphocytes and macrophages. *J. Virol.* 77, 2539–2549.

Fruman, D.A., Snapper, S.B., Yballe, C.M., Davidson, L., Yu, J.Y., Alt, F.W., and Cantley, L.C. (1999). Impaired B cell development and proliferation in absence of phosphoinositide 3-kinase p85alpha. *Science* 283, 393–397.

Gauduin, M.C., Yu, Y., Barabasz, A., Carville, A., Piatak, M., Lifson, J.D., Desrosiers, R.C., and Johnson, R.P. (2006). Induction of a virus-specific effector-memory CD4+ T cell response by attenuated SIV infection. *J. Exp. Med.* 203, 2661–2672.

Geyer, M., Fackler, O.T., and Peterlin, B.M. (2001). Structure--function relationships in HIV-1 Nef. *EMBO Rep.* 2, 580–585.

Gitlin, A.D., Shulman, Z. and Nussenzweig, M.C. (2014). Clonal selection in the germinal centre by regulated proliferation and hypermutation. *Nature* 509, 637–640.

Gray, E.S., Madiga, M.C., Hermanus, T., Moore, P.L., Wibmer, C.K., Tumba, N.L., Werner, L., Mlisana, K., Sibeko, S., Williamson, C., et al. (2011). The neutralization breadth of HIV-1 develops incrementally over four years and is associated with CD4+ T cell decline and high viral load during acute infection. *J. Virol.* 85, 4828–4840.

Haigwood, N.L., Watson, A., Sutton, W.F., McClure, J., Lewis, A., Ranchalis, J., Travis, B., Voss, G., Letvin, N.L., Hu, S.L., et al. (1996). Passive immune globulin therapy in the SIV/macaque model: early intervention can alter disease profile. *Immunol. Lett.* 51, 107–114.

Haralick, R.M., Shanmugam, K., and Dinstein, I. (1973) Textural features for image classification. *IEEE Transactions on Systems, Man, and Cybernetics* SMC-3, 610–621.

Hashimoto, M., Bhuyan, F., Hiyoshi, M., Noyori, O., Nasser, H., Miyazaki, M., Saito, T., Kondoh, Y., Osada, H., Kimura, S., et al. (2016). Potential role of the formation of tunneling nanotubes in HIV-1 spread in macrophages. *J. Immunol.* 196, 1832–1841.

Hau, T.T.T., Nishizawa, M., Harada, S., Phan, M.H., Kanno, Y., Nomura, T., Matsuoka, S., Kawana-Tachikawa, A., Hall, W.W., Matano, T., et al. (2022). Association of envelope-specific B-cell differentiation and viral selective pressure signatures in HIV-1 CRF01_AE infection. *AIDS* 36, 1629–1641.

Havenar-Daughton, C., Carnathan, D.G., Torrents de la Peña, A., Pauthner, M., Briney, B., Reiss, S.M., Wood, J.S., Kaushik, K., van Gils, M.J., Rosales, S.L., et al. (2016). Direct Probing of Germinal Center Responses Reveals Immunological Features and Bottlenecks for Neutralizing Antibody Responses to HIV Env Trimer. *Cell Rep.* 17, 2195–2209.

Hoof, I., Peters, B., Sidney, J., Pedersen, L.E., Sette, A., Lund, O., Buus, S., and Nielsen, M.. (2009). NetMHCpan, a method for MHC class I binding prediction beyond humans. *Immunogenetics* 61, 1–13.

Hunziker, L., Recher, M., Macpherson, A.J., Ciurea, A., Freigang, S., Hengartner, H., and Zinkernagel, R.M. (2003). Hypergammaglobulinemia and autoantibody induction mechanisms in viral infections. *Nat. Immunol.* 4, 343–349.

Iseda, S., Takahashi, N., Poplimont, H., Nomura, T., Seki, S., Nakane, T., Nakamura, M., Shi, S., Ishii, H., Furukawa, S., et al. (2016). Biphasic CD8+ T-cell defense in simian

immunodeficiency virus control by acute-phase passive neutralizing antibody immunization. *J. Virol.* 90, 6276–6290.

Ishii, H., Kawada, M., Tsukamoto, T., Yamamoto, H., Matsuoka, S., Shiino, T., Takeda, A., Inoue, M., Iida, A., Hara, H., et al. (2012). Impact of vaccination on cytotoxic T lymphocyte immunodominance and cooperation against simian immunodeficiency virus replication in rhesus macaques. *J. Virol.* 86, 738–745.

Iwamoto, N., Takahashi, N., Seki, S., Nomura, T., Yamamoto, H., Inoue, M., Shu, T., Naruse, T.K., Kimura, A., and Matano, T. (2014). Control of simian immunodeficiency virus replication by vaccine-induced Gag- and Vif-specific $CD8^+$ T cells. *J. Virol.* 88, 425–433.

Jia, B., Serra-Moreno, R., Neidermyer, W., Rahmberg, A., Mackey, J., Fofana, I.B., Johnson, W.E., Westmoreland, S., and Evans, D.T. (2009). Species-specific activity of SIV Nef and HIV-1 Vpu in overcoming restriction by tetherin/BST2. *PLoS Pathog.* 5, e1000429.

Joas, S., Sauermann, U., Roshani, B., Klippert, A., Daskalaki, M., Mätz-Rensing, K., Stolte-Leeb, N., Heigele, A., Tharp, G.K., Gupta, P.M., et al. (2020). Nef-Mediated CD3-TCR Downmodulation Dampens Acute Inflammation and Promotes SIV Immune Evasion. *Cell Rep.* 30, 2261–2274.e7.

Junt, T., Moseman, E.A., Iannacone, M., Massberg, S., Lang, P.A., Boes, M., Fink, K., Henrickson, S.E., Shayakhmetov, D.M., Di Paolo, N.C., et al. (2007). Subcapsular sinus macrophages in lymph nodes clear lymph-borne viruses and present them to antiviral B cells. *Nature* 450, 110–114.

Kawada, M., Tsukamoto, T., Yamamoto, H., Takeda, A., Igarashi, H., Watkins, D.I., and Matano, T. (2007). Long-term control of simian immunodeficiency virus replication with central memory

CD4+ T-cell preservation after nonsterile protection by a cytotoxic T-lymphocyte-based vaccine. *J. Virol.* 81, 5202–5211.

Kennedy, S.G., Wagner, A.J., Conzen, S.D., Jordán, J., Bellacosa, A., Tsichlis, P.N., and Hay, N. (1997). The PI 3-kinase/Akt signaling pathway delivers an anti-apoptotic signal. *Genes Dev.* 11, 701–713.

Kestler, H.W. 3rd, Ringler, D.J., Mori, K., Panicali, D.L., Sehgal, P.K., Daniel, M.D., and Desrosiers, R.C. (1991). Importance of the nef gene for maintenance of high virus loads and for development of AIDS. *Cell* 65, 651–662.

Kim, D.H., Sarbassov, D.D., Ali, S.M., Latek, R.R., Guntur, K.V., Erdjument-Bromage, H., Tempst, P., and Sabatini, D.M. (2003). GbetaL, a positive regulator of the rapamycin-sensitive pathway required for the nutrient-sensitive interaction between raptor and mTOR. *Mol. Cell* 11, 895–904.

Kirchhoff, F., Greenough, T.C., Brettler, D.B., Sullivan, L.L. and Desrosiers, R.C. (1995). Absence of intact nef sequences in a long-term, nonprogressing survivor of HIV-1 infection. N. Engl. J. Med. *332*, 228–232.

Kumar, A., Abbas, W., Colin, L., Khan, K.A., Bouchat, S., Varin, A., Larbi, A., Gatot, J.S., Kabeya, K., Vanhulle, C., et al. (2016). Tuning of AKT-pathway by Nef and its blockade by protease inhibitors results in limited recovery in latently HIV infected T-cell line. *Sci. Rep.* 6, 24090.

Kumar, V., Scandella, E., Danuser, R., Onder, L., Nitschké, M., Fukui, Y., Halin, C., Ludewig, B., and Stein, J.V. (2010). Global lymphoid tissue remodeling during a viral infection is orchestrated by a B cell-lymphotoxin-dependent pathway. *Blood* 115, 4725–4733.

Leuchowius, K.J., Weibrecht, I., Landegren, U., Gedda, L., and Söderberg, O. (2009). Flow cytometric in situ proximity ligation analyses of protein interactions and post-translational modification of the epidermal growth factor receptor family. *Cytometry A* 75, 833–839.

Levesque, M.C., Moody, M.A., Hwang, K.K., Marshall, D.J., Whitesides, J.F., Amos, J.D., Gurley, T.C., Allgood, S., Haynes, B.B., Vandergrift, N.A., et al. (2009). Polyclonal B cell differentiation and loss of gastrointestinal tract germinal centers in the earliest stages of HIV-1 infection. *PLoS Med.* 6, e1000107.

Lichterfeld, M., Kavanagh, D.G., Williams, K.L., Moza, B., Mui, S.K., Miura, T., Sivamurthy, R., Allgaier, R., Pereyra, F., Trocha, A., et al. (2007). A viral CTL escape mutation leading to immunoglobulin-like transcript 4-mediated functional inhibition of myelomonocytic cells. *J. Exp. Med.* 204, 2813–2824.

Limon, J.J., So, L., Jellbauer, S., Chiu, H., Corado, J., Sykes, S.M., Raffatellu, M., and Fruman, D.A. (2014). mTOR kinase inhibitors promote antibody class switching via mTORC2 inhibition. *Proc. Natl. Acad. Sci. USA* 111, E5076–5085.

Lindqvist, M., van Lunzen, J., Soghoian, D.Z., Kuhl, B.D., Ranasinghe, S., Kranias, G., Flanders, M.D., Cutler, S., Yudanin, N., Muller, M.I., et al. (2012). Expansion of HIV-specific T follicular helper cells in chronic HIV infection. *J. Clin. Invest.* 122, 3271–3280.

Locci, M., Havenar-Daughton, C., Landais, E., Wu, J., Kroenke, M.A., Arlehamn, C.L., Su, L.F., Cubas, R., Davis, M.M., Sette, A., et al. (2013). Human circulating PD-1+CXCR3-CXCR5+ memory Tfh cells are highly functional and correlate with broadly neutralizing HIV antibody responses. *Immunity* 39, 758–769.

Lucas, C.L., Kuehn, H.S., Zhao, F., Niemela, J.E., Deenick, E.K., Palendira, U., Avery, D.T., Moens, L., Cannons, J.L., Biancalana, M., et al. (2014). Dominant-activating germline mutations in the gene encoding the PI(3)K catalytic subunit p110δ result in T cell senescence and human immunodeficiency. *Nat. Immunol.* 15*,* 88–97.

Luo, W., Hawse, W., Conter, L., Trivedi, N., Weisel, F., Wikenheiser, D., Cattley, R.T., and Shlomchik, M.J. (2019). The AKT kinase signaling network is rewired by PTEN to control proximal BCR signaling in germinal center B cells. *Nat. Immunol.* 20, 736–746.

Marzec, M., Liu, X., Kasprzycka, M., Witkiewicz, A., Raghunath, P.N., El-Salem, M., Robertson, E., Odum, N., and Wasik, M.A. (2008). IL-2- and IL-15-induced activation of the rapamycin-sensitive mTORC1 pathway in malignant CD4+ T lymphocytes. *Blood* 111, 2181–2189.

Mason, R.D., Welles, H.C., Adams, C., Chakrabarti, B.K., Gorman, J., Zhou, T., Nguyen, R., O'Dell, S., Lusvarghi, S., Bewley, C.A., et al. (2016). Targeted Isolation of Antibodies Directed against Major Sites of SIV Env Vulnerability. *PLoS Pathog.* 12, e1005537.

Matano, T., Kobayashi, M., Igarashi, H., Takeda, A., Nakamura, H., Kano, M., Sugimoto, C., Mori, K., Iida, A., Hirata, T., et al. (2004). Cytotoxic T lymphocyte-based control of simian immunodeficiency virus replication in a preclinical AIDS vaccine trial. *J. Exp. Med.* 199, 1709–1718.

Mattapallil, J.J., Douek, D.C., Hill, B., Nishimura, Y., Martin, M., and Roederer, M. (2005). Massive infection and loss of memory CD4+ T cells in multiple tissues during acute SIV infection. *Nature* 434, 1093–1097.

Mikell, I., Sather, D.N., Kalams, S.A., Altfeld, M., Alter, G., and Stamatatos, L. (2011). Characteristics of the earliest cross-neutralizing antibody response to HIV-1. *PLoS Pathog.* 7, e1001251.

Moir, S., Malaspina, A., Ogwaro, K.M., Donoghue, E.T., Hallahan, C.W., Ehler, L.A., Liu, S., Adelsberger, J., Lapointe, R., Hwu, P., et al. (2001). HIV-1 induces phenotypic and functional perturbations of B cells in chronically infected individuals. *Proc. Natl. Acad. Sci. USA* 98, 10362–10367.

Moody, M.A., Pedroza-Pacheco, I., Vandergrift, N.A., Chui, C., Lloyd, K.E., Parks, R., Soderberg, K.A., Ogbe, A.T., Cohen, M.S., Liao, H.X., Gao, F., et al. (2016). Immune perturbations in HIV-1-infected individuals who make broadly neutralizing antibodies. *Sci. Immunol.* 1, aag0851.

Moore, P.L., Gray, E.S., Wibmer, C.K., Bhiman, J.N., Nonyane, M., Sheward, D.J., Hermanus, T., Bajimaya, S., Tumba, N.L., Abrahams, M.R., et al. (2012). Evolution of an HIV glycan-dependent broadly neutralizing antibody epitope through immune escape. *Nat. Med.* 18, 1688–1692.

Nakane, T., Nomura, T., Shi, S., Nakamura, M., Naruse, T.K., Kimura, A., Matano, T., and Yamamoto, H. (2013). Limited impact of passive non-neutralizing antibody immunization in acute SIV infection on viremia control in rhesus macaques. *PLoS ONE* 8, e73453.

Naruse, T.K., Chen, Z., Yanagida, R., Yamashita, T., Saito, Y., Mori, K., Akari, H., Yasutomi, Y., Miyazawa, M., Matano, T., et al. (2010). Diversity of MHC class I genes in Burmese-origin rhesus macaques. *Immunogenetics* 62, 601–611.

Ng, C.T., Jaworski, J.P., Jayaraman, P., Sutton, W.F., Delio, P., Kuller, L., Anderson, D., Landucci, G., Richardson, B.A., Burton, D.R., et al. (2010). Passive neutralizing antibody controls SHIV viremia and enhances B cell responses in infant macaques. *Nat. Med.* 16, 1117–1119.

Nguyen, H., Ramana, C.V., Bayes, J., and Stark, G.R. (2001). Roles of phosphatidylinositol 3-kinase in interferon-gamma-dependent phosphorylation of STAT1 on serine 727 and activation of gene expression. *J. Biol. Chem.* 276, 33361–33368.

Nishimura, Y., Gautam, R., Chun, T.W., Sadjadpour, R., Foulds, K.E., Shingai, M., Klein, F., Gazumyan, A., Golijanin, J., Donaldson, M., et al. (2017). Early antibody therapy can induce long-lasting immunity to SHIV. *Nature* 543, 559–563.

Nomura, T., Yamamoto, H., Shiino, T., Takahashi, N., Nakane, T., Iwamoto, N., Ishii, H., Tsukamoto, T., Kawada, M., Matsuoka, S., et al. (2012). Association of major histocompatibility complex class I haplotypes with disease progression after simian immunodeficiency virus challenge in Burmese rhesus macaques. *J. Virol.* 86, 6481–6490.

Nutt, S.L., Hodgkin, P.D., Tarlinton, D.M., and Corcoran, L.M. (2015). The generation of antibody-secreting plasma cells. *Nat. Rev. Immunol.* 15, 160–171.

Omori, S.A., Cato, M.H., Anzelon-Mills, A., Puri, K.D., Shapiro-Shelef, M., Calame, K., and Rickert, R.C. (2006). Regulation of class-switch recombination and plasma cell differentiation by phosphatidylinositol 3-kinase signaling. *Immunity* 25, 545–557.

Perfetto, S.P., Chattopadhyay, P.K., Lamoreaux, L., Nguyen, R., Ambrozak, D., Koup, R.A., and Roederer, M. (2006). Amine reactive dyes: an effective tool to discriminate live and dead cells in polychromatic flow cytometry. *J. Immunol. Methods* 313, 199–208.

Petrovas, C., Yamamoto, T., Gerner, M.Y., Boswell, K.L., Wloka, K., Smith, E.C., Ambrozak, D.R., Sandler, N.G., Timmer, K.J., Sun, X., et al. (2012). CD4 T follicular helper cell dynamics during SIV infection. *J. Clin. Invest.* 122, 3281–3294.

Qiao, X., He, B., Chiu, A., Knowles, D.M., Chadburn, A., and Cerutti, A. (2006). Human immunodeficiency virus 1 Nef suppresses CD40-dependent immunoglobulin class switching in bystander B cells. *Nat. Immunol.* 7, 302–310.

Ray, J.P., Staron, M.M., Shyer, J.A., Ho, P.C., Marshall, H.D., Gray, S.M., Laidlaw, B.J., Araki, K., Ahmed, R., Kaech, S.M., et al. (2015). The interleukin-2-mTORc1 kinase axis defines the signaling, differentiation, and metabolism of T helper 1 and follicular B helper T cells. *Immunity* 43, 690–702.

Recher, M., Lang, K.S., Hunziker, L., Freigang, S., Eschli, B., Harris, N.L., Navarini, A., Senn, B.M., Fink, K., Lötscher, M., et al. (2004). Deliberate removal of T cell help improves virus-neutralizing antibody production. *Nat. Immunol.* 5, 934–942.

Recher, M., Lang, K.S., Navarini, A., Hunziker, L., Lang, P.A., Fink, K., Freigang, S., Georgiev, P., Hangartner, L., Zellweger, R., et al. (2007). Extralymphatic virus sanctuaries as a consequence of potent T-cell activation. *Nat. Med.* 13, 1316–1323.

Rickles, R.J., Botfield, M.C., Weng, Z., Taylor, J.A., Green, O.M., Brugge, J.S., and Zoller, M.J. (1994). Identification of Src, Fyn, Lyn, PI3K and Abl SH3 domain ligands using phage display libraries. *EMBO J.* 13, 5598–5604.

Sammicheli, S., Kuka, M., Di Lucia, P., de Oya, N.J., De Giovanni, M., Fioravanti, J., Cristofani, C., Maganuco, C.G., Fallet, B., Ganzer, L., et al. (2016). Inflammatory monocytes hinder antiviral B cell responses. *Sci. Immunol.* 1, pii: eaah6789.

Sander, S., Chu, V.T., Yasuda, T., Franklin, A., Graf, R., Calado, D.P., Li, S., Imami, K., Selbach, M., Di Virgilio, M., et al. (2015). PI3 kinase and FOXO1 transcription factor activity differentially control B cells in the germinal center light and dark zones. *Immunity* 43, 1075–1086.

Sarbassov, D.D., Guertin, D.A., Ali, S.M., and Sabatini, D.M. (2005) Phosphorylation and regulation of Akt/PKB by the rictor-mTOR complex. *Science* 307, 1098–1101.

Schindler, M., Münch, J., Brenner, M., Stahl-Hennig, C., Skowronski, J., and Kirchhoff, F. (2004). Comprehensive analysis of nef functions selected in simian immunodeficiency virus-infected macaques. *J. Virol.* 78, 10588–10597.

Sette A, Sidney J, Southwood S, Moore C, Berry J, Dow C, Bradley K, Hoof I, Lewis MG, Hildebrand WH et al. (2012). A shared MHC supertype motif emerges by convergent evolution in macaques and mice, but is totally absent in human MHC molecules. *Immunogenetics* 64, 421–434.

Shi, S., Seki, S., Matano, T., and Yamamoto, H. (2013). IL-21-producer CD4+ T cell kinetics during primary simian immunodeficiency virus infection. *Microbes Infect.* 15, 697–707.

Shulman, Z., Gitlin, A.D., Weinstein, J.S., Lainez, B., Esplugues, E., Flavell, R.A., Craft, J.E., and Nussenzweig, M.C. (2014). Dynamic signaling by T follicular helper cells during germinal center B cell selection. *Science* 345, 1058–1062.

Silveira, E.L., Kasturi, S.P., Kovalenkov, Y., Rasheed, A.U., Yeiser, P., Jinnah, Z.S., Legere, T.H., Pulendran, B., Villinger, F., and Wrammert, J. (2015). Vaccine-induced plasmablast responses in rhesus macaques: phenotypic characterization and a source for generating antigen-specific monoclonal antibodies. *J. Immunol. Methods* 416, 69–83.

Sommerstein, R., Flatz, L., Remy, M.M., Malinge, P., Magistrelli, G., Fischer, N., Sahin, M., Bergthaler, A., Igonet, S., Ter Meulen, J., et al. (2015). Arenavirus glycan shield promotes neutralizing antibody evasion and protracted infection. *PLoS Pathog.* 11, e1005276.

Srinivasan, L., Sasaki, Y., Calado, D.P., Zhang, B., Paik, J.H., DePinho, R.A., Kutok, J.L., Kearney, J.F., Otipoby, K.L., and Rajewsky, K. (2009). PI3 kinase signals BCR-dependent mature B cell survival. *Cell* 139, 573–586.

Stolp, B., Imle, A., Coelho, F.M., Hons, M., Gorina, R., Lyck, R., Stein, J.V., and Fackler, O.T.. (2012). HIV-1 Nef interferes with T-lymphocyte circulation through confined environments in vivo. *Proc. Natl. Acad. Sci. USA* 109, 18541–18546.

Swingler, S., Zhou, J., Swingler, C., Dauphin, A., Greenough, T., Jolicoeur, P., and Stevenson, M. (2008). Evidence for a pathogenic determinant in HIV-1 Nef involved in B cell dysfunction in HIV/AIDS. *Cell Host Microbe* 4, 63–76.

Takahashi, N., Nomura, T., Takahara, Y., Yamamoto, H., Shiino, T., Takeda, A., Inoue, M., Iida, A., Hara,H., Shu, T., et al. (2013). A novel protective MHC-I haplotype not associated with dominant Gag-specific $CD8^+$ T-cell responses in SIV_{mac239} infection of Burmese rhesus macaques. *PLoS ONE* 8, e54300.

Terahara, K., Ishii, H., Nomura, T., Takahashi, N., Takeda, A., Shiino, T., Tsunetsugu-Yokota, Y., and Matano, T. (2014). Vaccine-induced CD107a+ CD4+ T cells are resistant to depletion following AIDS virus infection. *J. Virol.* 88, 14232–14240.

Tomaras, G.D., Yates, N.L., Liu, P., Qin, L., Fouda, G.G., Chavez, L.L., Decamp, A.C., Parks, R.J., Ashley, V.C., Lucas, J.T., et al. (2008). Initial B-cell responses to transmitted human immunodeficiency virus type 1: virion-binding immunoglobulin M (IgM) and IgG antibodies followed by plasma anti-gp41 antibodies with ineffective control of initial viremia. *J. Virol.* 82, 12449–12463.

Wang, J., Sohn, H., Sun, G., Milner, J.D. and Pierce, S.K. (2014). The autoinhibitory C-terminal SH2 domain of phospholipase C-γ2 stabilizes B cell receptor signalosome assembly. *Sci. Signal.* 7, ra89.

Xu, W., Santini, P.A., Sullivan, J.S., He, B., Shan, M., Ball, S.C., Dyer, W.B., Ketas, T.J., Chadburn, A., Cohen-Gould, L., et al. (2009). HIV-1 evades virus-specific IgG2 and IgA responses by targeting systemic and intestinal B cells via long-range intercellular conduits. *Nat. Immunol.* 10, 1008–1017.

Yamamoto, H., Kawada, M., Takeda, A., Igarashi, H. and Matano, T. (2007). Post-infection immunodeficiency virus control by neutralizing antibodies. *PLoS ONE 2*, e540.

Zhang, F., Wilson, S.J., Landford, W.C., Virgen, B., Gregory, D., Johnson, M.C., Munch, J., Kirchhoff, F., Bieniasz, P.D., and Hatziioannou, T. (2009). Nef proteins from simian immunodeficiency viruses are tetherin antagonists. *Cell Host Microbe 6*, 54–67.

Zotos, D., Coquet, J.M., Zhang, Y., Light, A., D'Costa, K., Kallies, A., Corcoran, L.M., Godfrey, D.I., Toellner, K.M., Smyth, M.J., et al. (2010). IL-21 regulates germinal center B cell

1178 differentiation and proliferation through a B cell-intrinsic mechanism. *J. Exp. Med.* 207, 365–
1179 378.
1180

1181 **Supplemental Information Legends**

1182

1183 **Fig. 1-Supplement 1. Profile of SIV_{mac239}-NAb non-inducer subgroup cohort.**

1184 Summary of a SIV_{mac239}-NAb non-inducer subgroup cohort (*n* = 19), composed from previously
1185 partially characterized, MHC class I haplotype-balanced naïve animals. Symbols A+, B+, E+,
1186 J+ and D+ represent possession of MHC-I haplotypes *90-120-Ia*, *90-120-Ib*, *90-010-Ie*, *90-*
1187 *088-Ij* and *90-010-Id*, respectively. For the titers, - represents negative; +/- represents
1188 neutralization in three out of four wells in a quadruplicate test. Gray shadings indicate
1189 euthanasia due to AIDS progression. Mamu-A and Mamu-B alleles of interest in this study are
1190 listed. These NAb non-inducers were previously partially reported for their plasma viral loads
1191 and MHC-I alleles (Nomura et al., 2012; Takahashi et al., 2013; Nakane et al., 2013; Iwamoto
1192 et al., 2014). R01-011 was previously partially reported for NAb titers measured with the same
1193 method using MT4 cells as targets (Kawada et al., 2007), which derived comparable results.

1194

1195 **Fig. 1-Supplement 2. IgG class-switched NAbs in the inducers.**

1196 Titration of SIV_{mac239}-neutralizing IgGs in the NAb inducers. SIV_{mac239}-specific IgGs, purified
1197 from pools of plasma with SIV_{mac239}-specific NAb titers, were obtained from each animal as
1198 described (Yamamoto et al., 2007) and examined for their neutralizing activity by 10 $TCID_{50}$
1199 SIV_{mac239} killing on MT4-R5 cells. NAb-negative anti-SIV IgG and control IgG were prepared
1200 from a representative animal (R01-011) with NAb-negative plasma and pooled plasma of
1201 uninfected rhesus macaques, respectively.

1202

1203 **Fig.1-Supplement 3. Anti-SIV binding IgG profiles in NAb inducers and non-inducers.**

1204 **(A)** Temporal changes in SIV_{mac251} Env gp120-specific antibody titers in the NAb non-inducers
1205 without rapid progression [NAb-negative non-rapid progressors, NAb(-) non-RPs] (left, *n* = 11)
1206 and NAb inducers [NAb(+)] (right, *n* = 9). NAb non-inducers showing rapid progression
1207 (euthanized with AIDS onset within approximately 1 year) were not included except for
1208 macaque R10-001 (shown in the left). Samples for non-RPs R06-001 and R10-002 were

unavailable.

(B) Unpaired t test of log-transformed anti-SIV Env Ab titers in NAb(-) non-RPs and NAb inducers. Bars represent geometric mean absorbance within each group.

(C) Lysed SIV_{mac} virion linear antigen-binding at year 1 p.i. in NAb(-) non-RPs and NAb inducers. Plasma anti-SIV_{mac251} IgGs were detected using a commercial western blotting system against the parental strain SIV_{mac251} (ZeptoMetrix). White arrowheads indicate Env gp120-specific bands. Experiments were performed twice with comparable results.

Fig. 1-Supplement 4. Env sequence variation pattern is not a major characteristic of NAb induction.

SIV_{mac239} Env sequence variations before and after NAb induction. For each animal, the upper time point shows pre-induction and the lower time point (in purple) shows post-induction (first or second time point with NAb titer > 1:2). Dominant residue changes are shown as follows: gp120 (gray), variable regions V1-V5 (blue), and gp41 (blue gray). Subdominant mutations are uncolored. Unlabeled gray and black shadings show subdominant and dominant deletion of residues. Parental SIV_{mac239} sequence is listed for V1-V5. Residues mutated in multiple animals within V1-V5 are shown in red.

Fig. 3-Supplement 1. Selection of Nef-G63E mutant SIV is linked with Nef_{62-70}-specific $CD8^+$ T-cell response positivity.

(A) Nef_{62-70}-specific CD8+ T-cell responses around week 20 post-SIV challenge in seven viremic NAb non-inducers possessing either of the MHC-I alleles Mamu-B*039:01, Mamu-B*004:01 or Mamu-A1*032:02.

(B) Temporal supernatant SIV p27 concentrations after wild type (WT) or Nef-G63E mutant SIV infection at multiplicity of infection (MOI) 0.001 on HSC-F cells. Data represent one of two independent experiments performed in triplicate. Bars: mean ± SEM.

(C) Comparison of plasma viral loads in Nef-G63E-selecting NAb non-inducers (n = 7) versus non-inducers at indicated time points post-SIV challenge. Bars represent geometric means.

log10-transformed values are compared by unpaired t tests.

Fig. 4-Supplement 1. Decreased Akt hyperactivation properties of Nef-G63E mutant SIV.

(A) Plasma ferritin levels (ng/ml) in examined NAb non-inducers versus Nef-G63E mutant SIV-selecting NAb inducers around year 1 post-infection. Bars represent mean in each group. Compared by unpaired t test.

(B) Relative levels of pAkt Ser473 (left panel) and threonine (Thr) 308 (right panel) in SIV Nef+ HSR5.4 cells (MOI 0.1, 4 days p.i.).

(C) Relative pAkt Ser473 levels in Nef+ HSC-F cells without stimuli and transiently pulsed with IFN-γ, IL-2 or SIV_{mac} Env gp130 after infection (MOI 0.2, 1 day).

(D) Gene expression significantly differing between WT and Nef-G63E SIV infection (MOI 5, 1 day). Black bars show potentially Akt-related genes. Asterisks show dynamics concordant with the Nef-G63E phenotype (PI3K-pAkt Ser473 downstream downregulation or inhibition upregulation).

(E) Representative flow cytometric gating (NAb inducer R01-012, wk 30 p.i.) of peripheral blood $CXCR3^{-}CXCR5^{+}PD\text{-}1^{+}$ memory follicular CD4+ T cells. Cells were gated as $CD3^{+}CD8^{-}CD4^{+}CD95^{+}CXCR5^{+}PD\text{-}1^{+}CXCR3^{-}$ live singlet PBMCs. Available samples of six NAb inducers showing peak Nef-G63E mutant selection around week 30 p.i. and thirteen viremic NAb non-inducers were tracked.

(F) Comparison of peripheral $CXCR3^{-}CXCR5^{+}PD\text{-}1^{+}$ memory Tfh cell frequencies between pre-SIV infection and around week 30 post-infection in NAb non-inducers developing disease before week 60 (left: n = 5) and alive more than 70 weeks (middle: n = 8) and Nef-G63E-detected NAb inducers alive more than 70 weeks (right: n = 6). Analyzed by Wilcoxon signed-rank tests.

MFIs relative to those in uninfected controls (%) are shown. **: $P < 0.01$, ***: $P < 0.001$, n.s.: not significant between WT and Nef-G63E mutant by unpaired t tests (B-C). Data represent one of two (B, C) independent experiments performed in triplicate (C: unstimulated) or quadruplicate (B, C: PI3K-pulsed). Bars: mean ± SEM.

Fig. 5-Supplement 1. Machine learning-verified morphological gating of Nef-invaded B cells *in vivo*.

(A) Representative gating strategy plus schematic of inguinal lymph node $Nef^{+}CD19^{+}$ B cells of an SIV_{mac239}-infected rhesus macaque analyzed by ImageStreamX MK II imaging flow cytometry (R10-012, week 160 p.i.). First-step incorporation of Live/Dead staining gates out $CD19^{+}$ B cells staining positive for Nef potentially due to pre-experimental membrane permeation (e.g., image #246896, #248952 and #71859). Second-step dual gating for intracellular Nef signal pixel Haralick variance mean (H Variance mean, X axis), a textural feature calculated from a gray level co-occurrence matrix (GLCM) for each image representing adjacent pixel signal strength heterogeneity and Nef signal intensity threshold (Y axis) gates out $CD19^{+}$ B cells showing potentially non-specific, strong intracellular binary clustered staining pixels for Nef deriving a large variance (X axis), and/or cells stained overtly strong for Nef and hence becoming void for feasible image verification (high threshold) (Y axis), both likely originating stochastically from post-experimental rupturing procedures including membrane permeation (e.g. image #18541). This two-step noise cancellation results in acquisition of a $Live/Dead^{-}$-Nef signal Haralick variance $mean^{lo}$-Nef signal intensity $threshold^{lo}$-$Nef^{+}CD19^{+}$ B-cell population (e.g. image #116318, #116250 and #132927) with a pericellular $Nef^{int\text{-}lo}$ staining, biologically concordant with Nef membrane anchoring, resembling Nef^{+} cells experimentally generated in vitro and showed the highest score in IDEAS6.3 machine learning module scoring for segregation of typical void vs. valid images (upper right). This gating was implemented for counting and analysis of Env-specific B-cell Nef invasion *in vivo* (Figure 5).

(B) Detection of contact-dependent Nef invasion from SIV-infected HSC-F $CD4^{+}$ T cells to cocultured Ramos B cells *in vitro*. Two typical images of an intercellular conduit (SSC, purple) with Nef (green) protrusions from infected HSC-F cells to $CD19^{+}$ (red) Ramos B cells from two independent experiments are shown.

Fig. 6-Supplement 1. Gating strategy of SIV_{mac239} Env gp140-specific B-cell responses.

Representative gating (R02-004, week 32 p.i.) of SIV Env gp140-specific memory B cells (B_{mem}) and plasmablasts (PBs). Two panels for PB gating are shown in lower resolution for visibility. B_{mem} staining was performed separately and gatings are merged with PB panels (second row, panels 2–4). For lineage-specific exclusion (first row, panel 4), CD10 was stained independently for B_{mem} (see parenthesis).

Figure 1

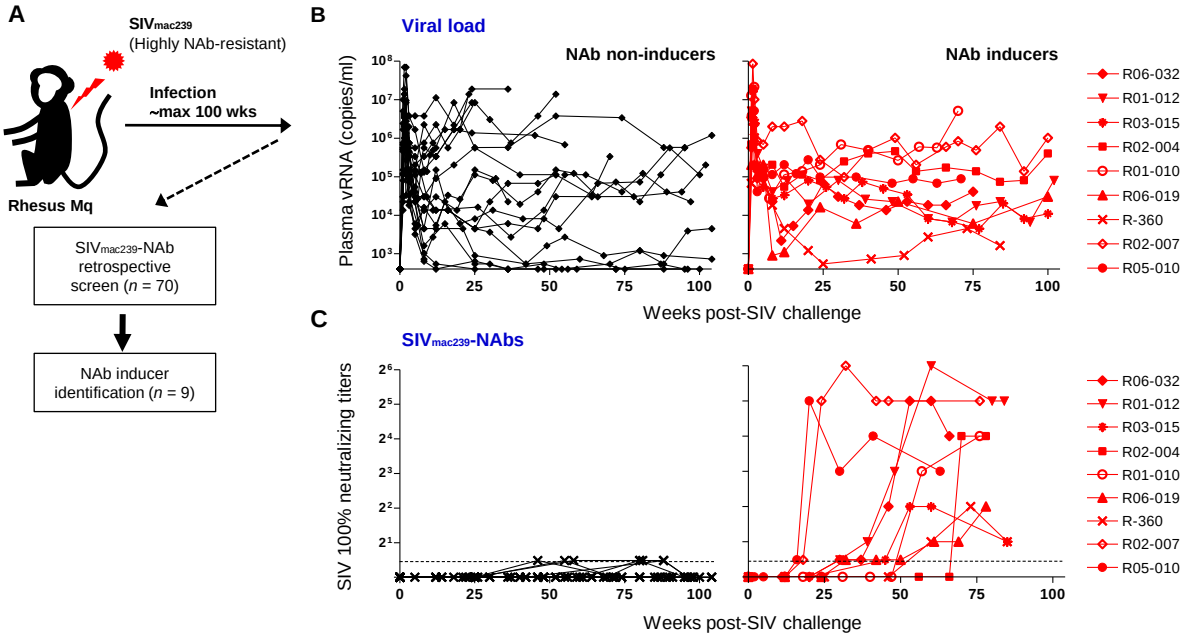
A
SIVmac239
(Highly NAb-resistant)
Infection
~max 100 wks
Rhesus Mq
SIVmac239-NAb
retrospective
screen (n = 70)
NAb inducer
identification (n = 9)
B
Viral load
NAb non-inducers
NAb inducers
Plasma vRNA (copies/ml)
Weeks post-SIV challenge
R06-032
R01-012
R03-015
R02-004
R01-010
R06-019
R-360
R02-007
R05-010
C
SIVmac239-NAbs
SIV 100% neutralizing titers
Weeks post-SIV challenge

Figure 2

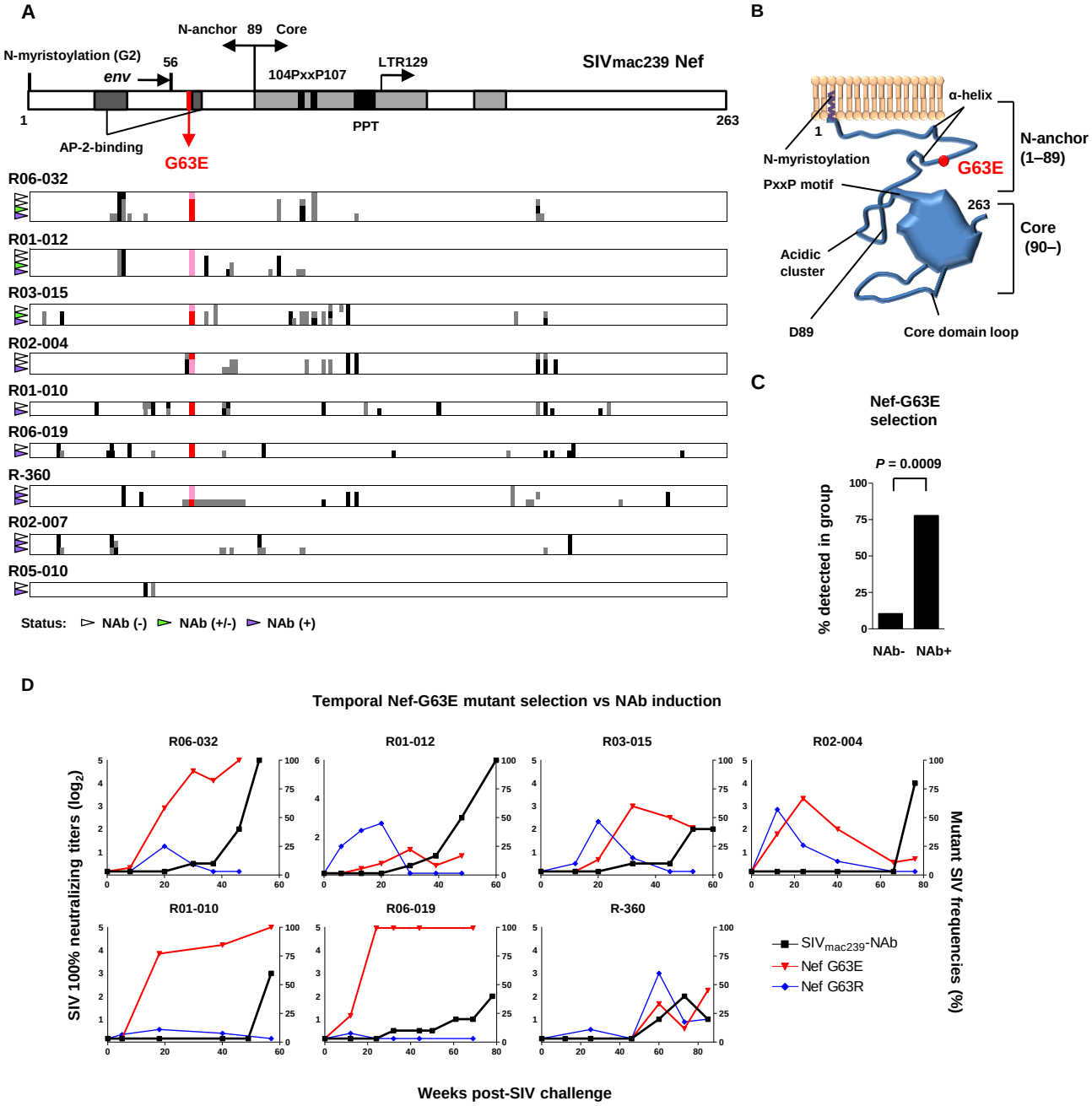
A
N-anchor 89 Core
N-myristoylation (G2)
56
env
104PxxP107
LTR129
SIVmac239 Nef
1
263
PPT
AP-2-binding
G63E
R06-032
R01-012
R03-015
R02-004
R01-010
R06-019
R-360
R02-007
R05-010
Status: NAb (-) NAb (+/-) NAb (+)
B
α-helix
1
N-anchor (1–89)
N-myristoylation
G63E
PxxP motif
263
Core (90–)
Acidic cluster
D89
Core domain loop
C
Nef-G63E selection
P = 0.0009
% detected in group
NAb-
NAb+
D
Temporal Nef-G63E mutant selection vs NAb induction
R06-032
R01-012
R03-015
R02-004
R01-010
R06-019
R-360
SIV 100% neutralizing titers (log2)
Mutant SIV frequencies (%)
SIVmac239-NAb
Nef G63E
Nef G63R
Weeks post-SIV challenge

Figure 3

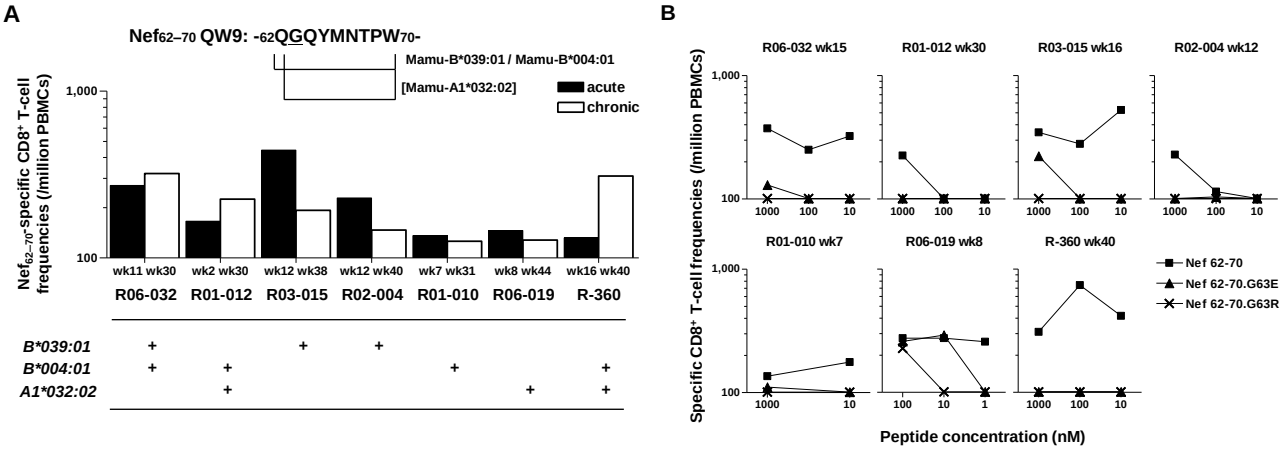
A
Nef62–70 QW9: -62QGQYMNTPW70-
Mamu-B*039:01 / Mamu-B*004:01
[Mamu-A1*032:02]
acute
chronic
Nef62–70-specific CD8+ T-cell frequencies (/million PBMCs)
1,000
100
wk11 wk30
wk2 wk30
wk12 wk38
wk12 wk40
wk7 wk31
wk8 wk44
wk16 wk40
R06-032
R01-012
R03-015
R02-004
R01-010
R06-019
R-360
B*039:01
B*004:01
A1*032:02
B
R06-032 wk15
R01-012 wk30
R03-015 wk16
R02-004 wk12
R01-010 wk7
R06-019 wk8
R-360 wk40
Nef 62-70
Nef 62-70.G63E
Nef 62-70.G63R
Specific CD8+ T-cell frequencies (/million PBMCs)
Peptide concentration (nM)

Figure 4

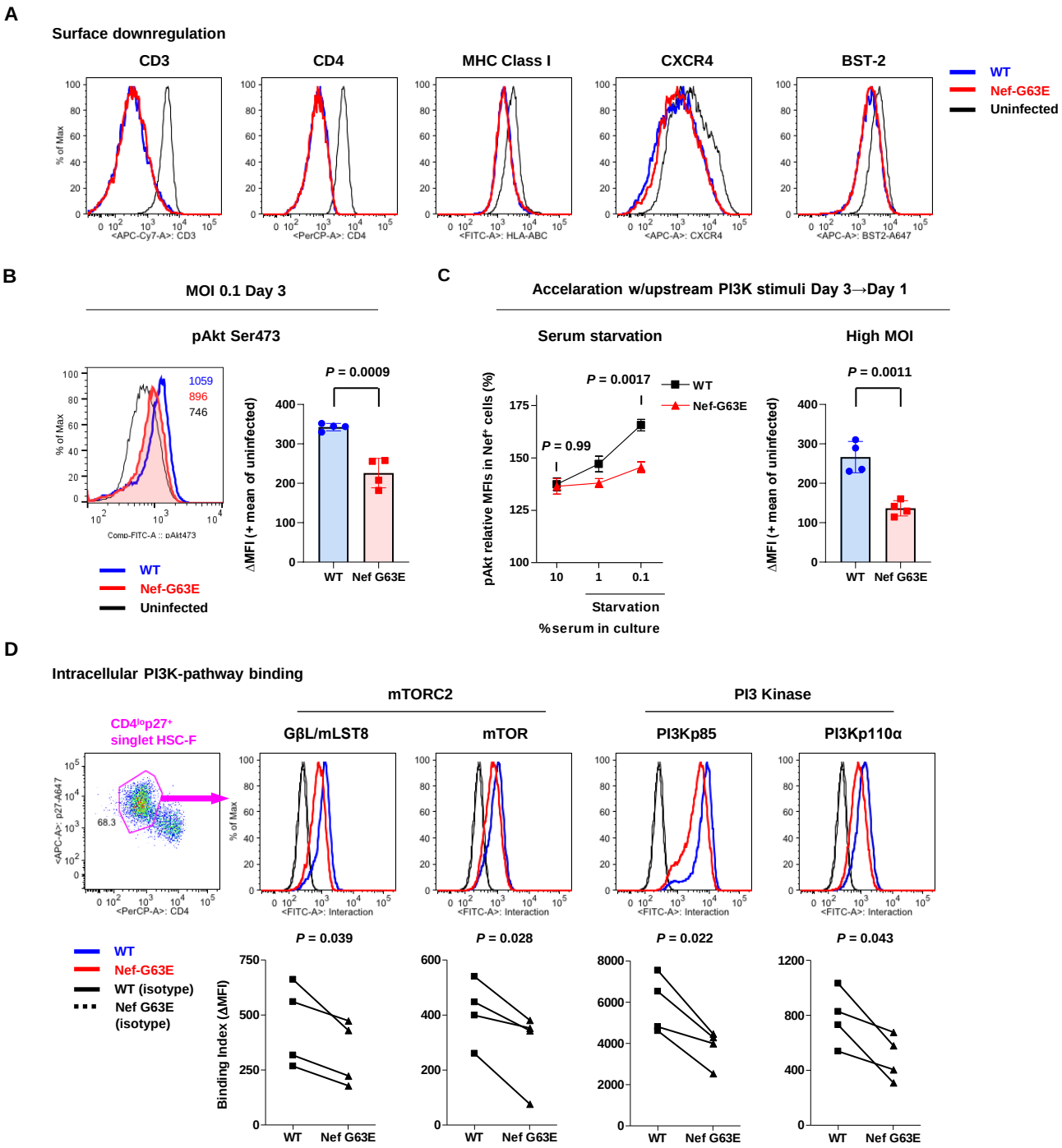
A
Surface downregulation
CD3
CD4
MHC Class I
CXCR4
BST-2
WT
Nef-G63E
Uninfected
% of Max
<APC-Cy7-A>: CD3
<PerCP-A>: CD4
<FITC-A>: HLA-ABC
<APC-A>: CXCR4
<APC-A>: BST2-A647
B
MOI 0.1 Day 3
pAkt Ser473
1059
896
746
Comp-FITC-A :: pAkt473
ΔMFI (+ mean of uninfected)
P = 0.0009
WT
Nef G63E
C
Accelaration w/upstream PI3K stimuli Day 3→Day 1
Serum starvation
High MOI
pAkt relative MFIs in Nef+ cells (%)
P = 0.0017
P = 0.99
Starvation
%serum in culture
P = 0.0011
D
Intracellular PI3K-pathway binding
mTORC2
PI3 Kinase
CD4lop27+
singlet HSC-F
68.3
<APC-A>: p27-A647
<PerCP-A>: CD4
GβL/mLST8
mTOR
PI3Kp85
PI3Kp110α
<FITC-A>: Interaction
WT (isotype)
Nef G63E (isotype)
Binding Index (ΔMFI)
P = 0.039
P = 0.028
P = 0.022
P = 0.043

Figure 5

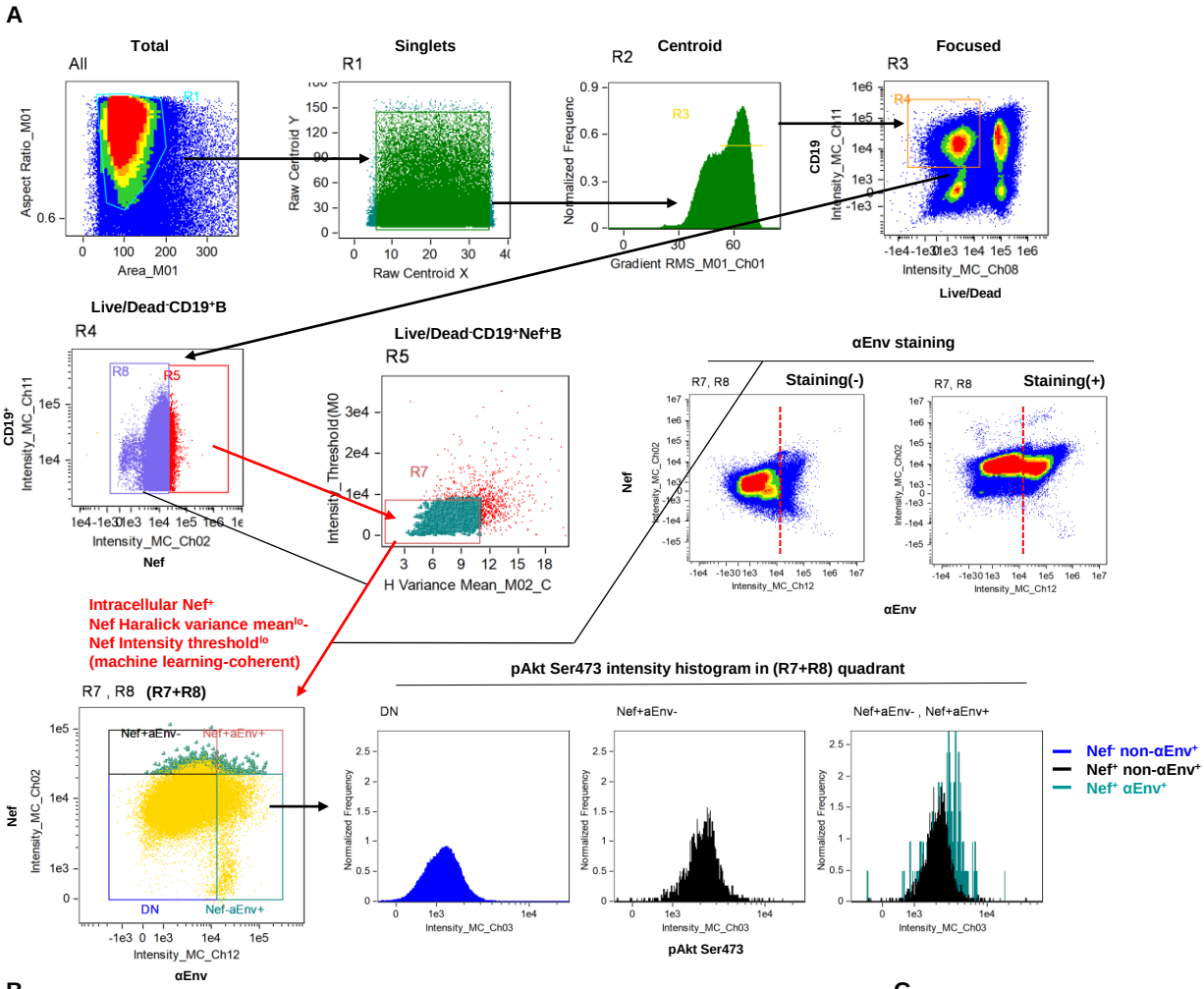
A
Total
All
Aspect Ratio_M01
Area_M01
Singlets
R1
Raw Centroid Y
Raw Centroid X
Centroid
R2
R3
Normalized Frequenc
Gradient RMS_M01_Ch01
Focused
R3
R4
CD19
Intensity_MC_Ch11
Intensity_MC_Ch08
Live/Dead
Live/Dead-CD19+B
R4
R8
R5
CD19+
Intensity_MC_Ch11
Intensity_MC_Ch02
Nef
Live/Dead-CD19+Nef+B
R5
R7
Intensity_Threshold(M0
H Variance Mean_M02_C
αEnv staining
R7, R8
Staining(-)
Staining(+)
Nef
Intensity_MC_Ch02
Intensity_MC_Ch12
αEnv
Intracellular Nef+
Nef Haralick variance meanlo-
Nef Intensity thresholdlo
(machine learning-coherent)
pAkt Ser473 intensity histogram in (R7+R8) quadrant
R7 , R8 (R7+R8)
Nef+aEnv-
Nef+aEnv+
DN
Nef-aEnv+
Nef
Intensity_MC_Ch02
Intensity_MC_Ch12
αEnv
DN
Nef+aEnv-
Nef+aEnv- , Nef+aEnv+
Normalized Frequency
Intensity_MC_Ch03
pAkt Ser473
Nef- non-αEnv+
Nef+ non-αEnv+
Nef+ αEnv+

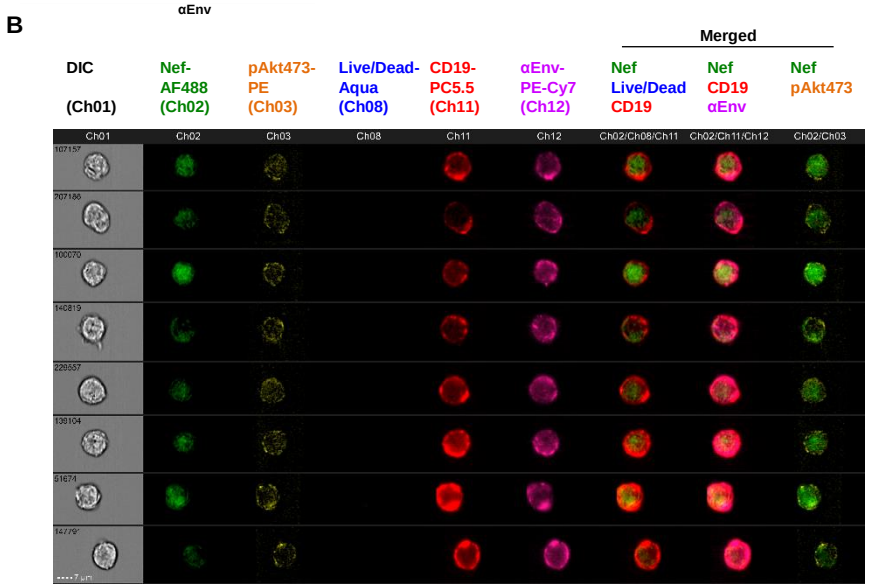
B
Merged
DIC (Ch01)
Nef-AF488 (Ch02)
pAkt473-PE (Ch03)
Live/Dead-Aqua (Ch08)
CD19-PC5.5 (Ch11)
αEnv-PE-Cy7 (Ch12)
Nef Live/Dead CD19
Nef CD19 αEnv
Nef pAkt473
Ch01
Ch02
Ch03
Ch08
Ch11
Ch12
Ch02/Ch08/Ch11
Ch02/Ch11/Ch12
Ch02/Ch03

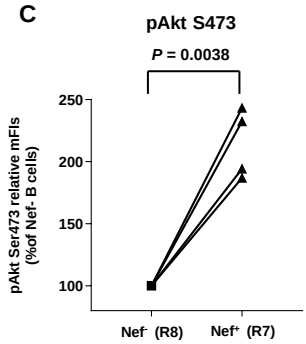
C
pAkt S473
P = 0.0038
pAkt Ser473 relative mFIs (%of Nef- B cells)
Nef- (R8)
Nef+ (R7)

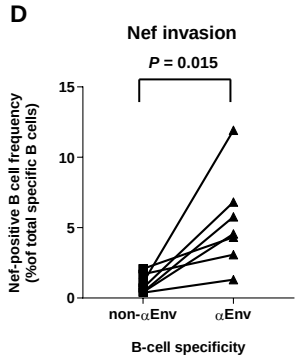
D
Nef invasion
P = 0.015
Nef-positive B cell frequency (%of total specific B cells)
non-αEnv
αEnv
B-cell specificity

Figure 6

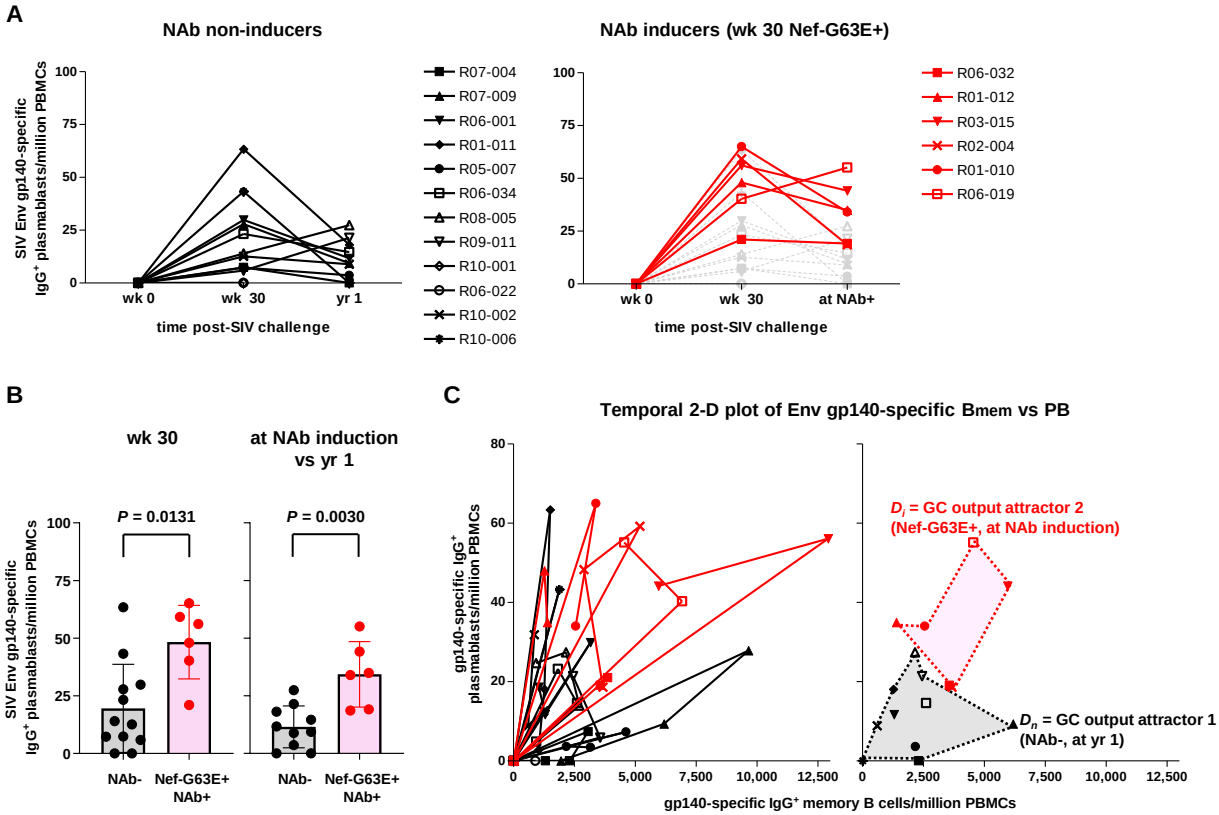
A
NAb non-inducers
NAb inducers (wk 30 Nef-G63E+)
SIV Env gp140-specific IgG+ plasmablasts/million PBMCs
time post-SIV challenge
wk 0
wk 30
yr 1
at NAb+
R07-004
R07-009
R06-001
R01-011
R05-007
R06-034
R08-005
R09-011
R10-001
R06-022
R10-002
R10-006
R06-032
R01-012
R03-015
R02-004
R01-010
R06-019
B
wk 30
at NAb induction vs yr 1
P = 0.0131
P = 0.0030
NAb-
Nef-G63E+ NAb+
C
Temporal 2-D plot of Env gp140-specific Bmem vs PB
gp140-specific IgG+ plasmablasts/million PBMCs
gp140-specific IgG+ memory B cells/million PBMCs
Dl = GC output attractor 2 (Nef-G63E+, at NAb induction)
Dn = GC output attractor 1 (NAb-, at yr 1)

NAb non-inducer cohort (*n* = 19)

MHC-I/ID	SIV$_{mac239}$ neutralization at 1:2 plasma dilution by 10TCID$_{50}$ killing assay (wks p.i.) wk11–20	wk21–30	wk31–40	wk41–50	wk51–60	wk61–70	wk71–80	wk81–90	wk91–104	pVL at 6 mo	Nef G63E at 1 yr	Detected *Mamu* alleles
A+												
R06-037		wk25 -		wk46 +/-			wk72 -	wk87 -	wk95 -	6.4×10^2	- (pVL < 400)	
R07-001		wk25 -		wk42 -				wk88 +/-	wk96 -	< 400	- (pVL < 400)	*A1*032:02*
R07-004		wk25 -		wk46 -		wk64 -	wk74 -	wk86 -		4.5×10^3	+	*B*039:01*
R07-009		wk25 -		wk46 -		wk64 -	wk74 -			4.5×10^3	-	
B+												
R06-001		wk25 -		wk48 -	wk60 -		wk80 -	wk90 -		8.2×10^3	-	
R06-039		wk25 -		wk46 -	wk56 -					8.5×10^6	-	*A1*032:02* , *B*004:01*
E+												
R01-011		wk22 -	wk40 -		wk52 -		wk71 -	wk85 -	wk104 -	1.3×10^5	-	*B*004:01*
R05-007		wk26 -			wk55 +/-		wk71 -	wk89 -	wk97 -	1.6×10^4	-	
R08-007		wk21 -		wk46 -		wk69 -		wk82 +/-		8.5×10^6	-	
R09-011	wk18 -		wk36 -		wk52 -					8.5×10^6	-	
R06-038		wk25 -			wk58 +/-		wk80 +/-		wk95 -	1.1×10^5	-	
J+												
R04-014	wk12 -	wk25 -	wk40 -							1.5×10^5	+ (wk40)	*B*039:01*
R06-022	wk12 -	wk23 -								1.4×10^7	- (wk23)	*B*039:01*
R10-001	wk14 -	wk30 -	wk37 -							1.9×10^7	- (wk37)	*B*039:01*
D+												
R05-006		wk25 -		wk48 -			wk80 -	wk90 -	wk98 -	5.4×10^2	-	*A1*032:02* , *B*004:01*
R06-034		wk25 -		wk42 -		wk61 -	wk80 +/-	wk88 +/-	wk96 -	4.5×10^3	-	*A1*032:02* , *B*004:01*
R08-005		wk25 -		wk48 -		wk68 -			wk100 -	9.0×10^2	-	*A1*032:02* , *B*004:01*
Others												
R10-002	wk14 -				wk59 -				wk104 -	5.7×10^5	-	
R10-006	wk14 -	wk30 -			wk55 -					1.0×10^6	-	

Fig. 1-Supplement 1.

Group	Rhesus ID	mg/ml (IgG)	Collected/pooled (wks post-challenge)	10 $TCID_{50}$ SIV_{mac239} 100% killing titer
NAb (+)	R06-032	30	wk 76	1:16
	R01-012	30	wk 73–87	1:32
	R03-015	30	wk 112	1:8
	R02-004	30	wk 76	1:4
	R01-010	30	wk 77	1:16
	R06-019	30	wk 85	1:4
	R-360	30	wk 60–86	1:4
	R02-007	30	wk 42–70	1:32
	R05-010	30	wk 71	1:64
NAb (-)	R01-011	42	wk 104	< 1:2
uninfected	pooled	36	-	< 1:2

Fig. 1-Supplement 2.

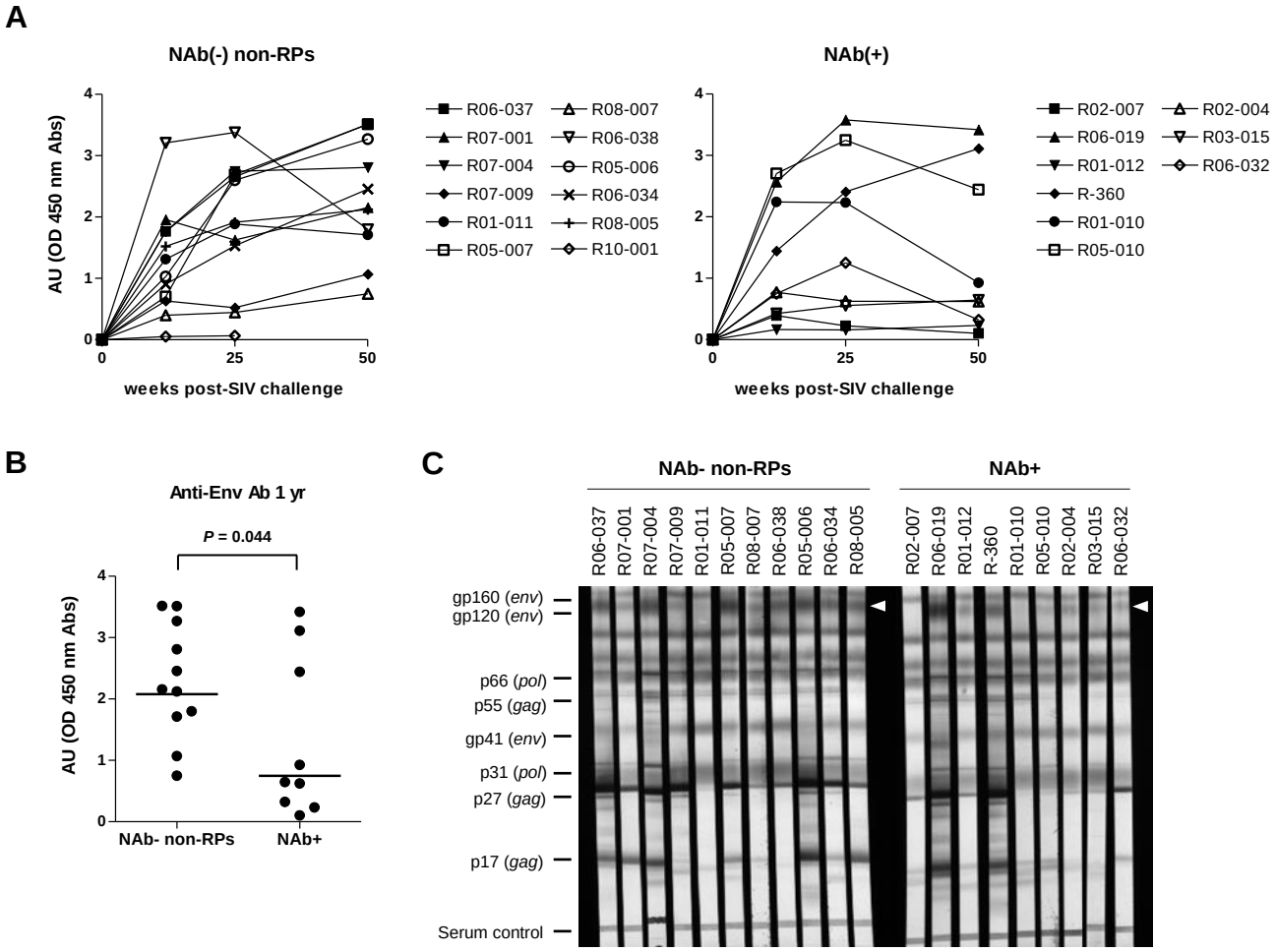

Fig.1-Supplement 3.

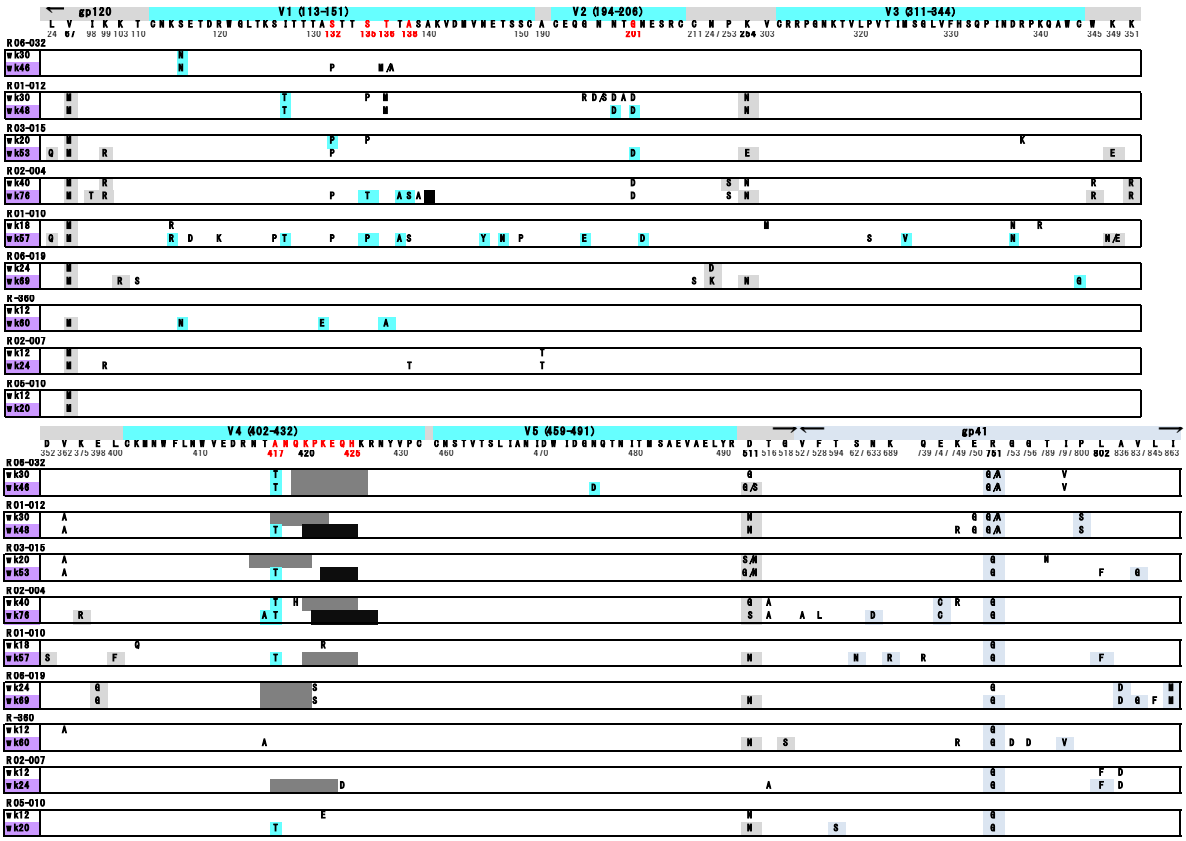

Fig. 1-Supplement 4.

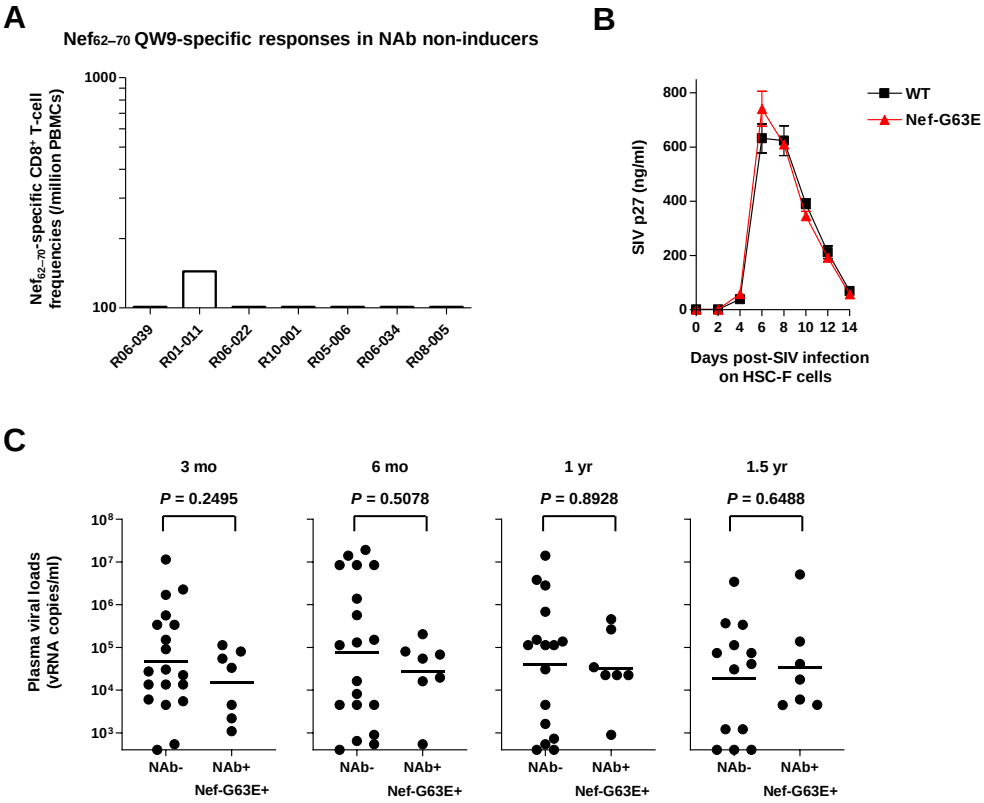

Fig. 3-Supplement 1.

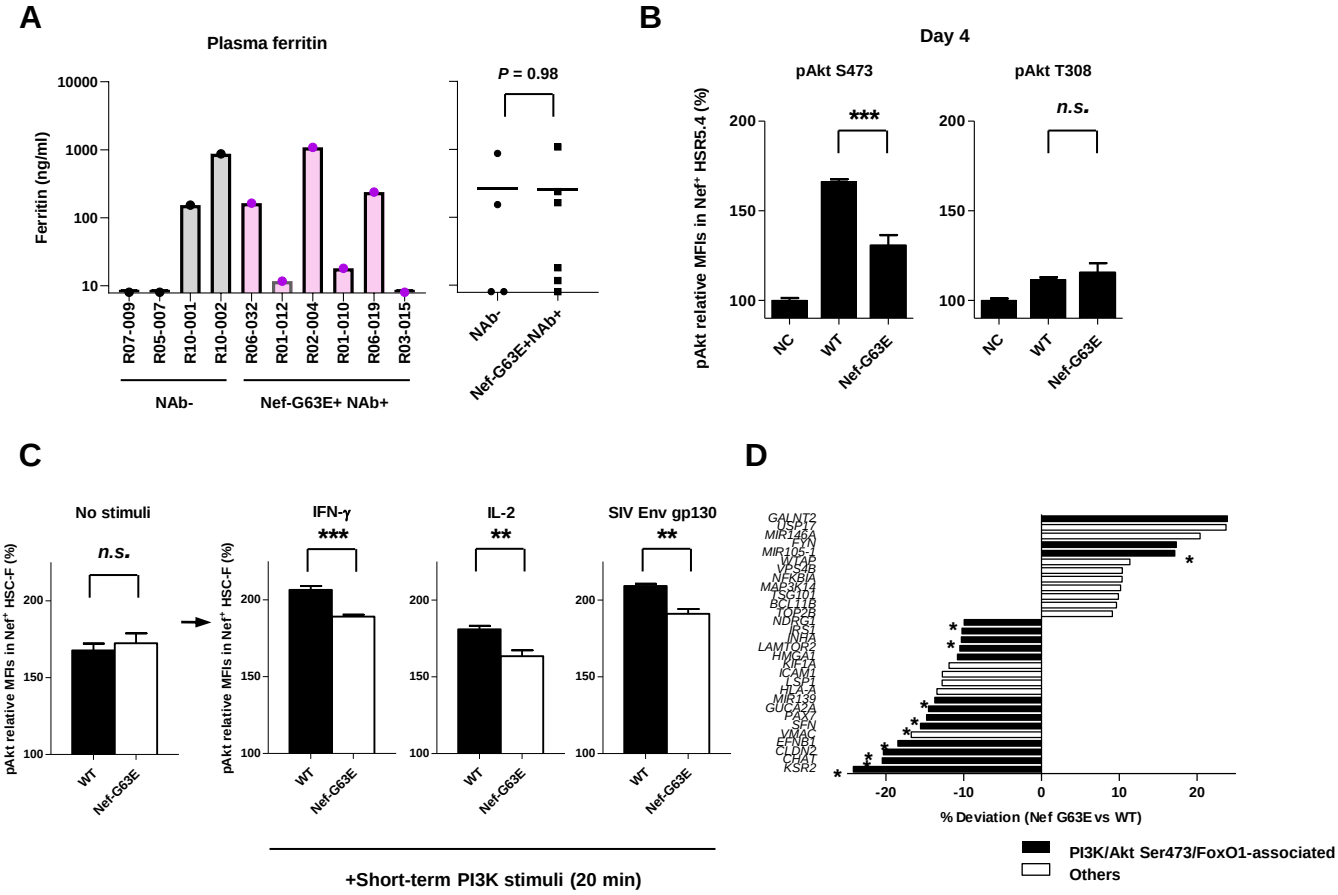

Fig. 4-Supplement 1.

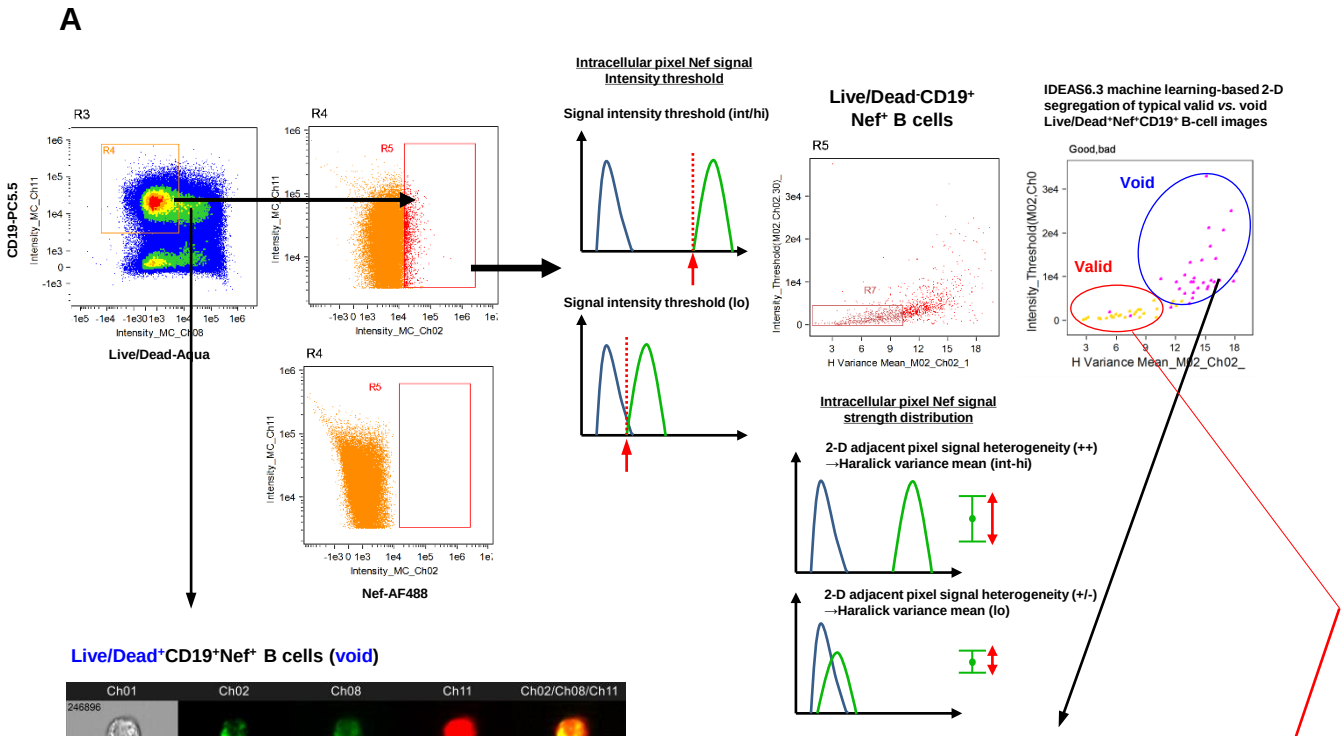

Live/Dead+CD19+Nef+ B cells (void)

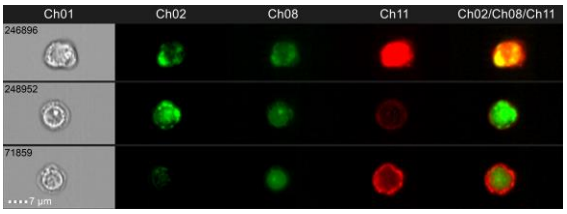

Live/Dead-CD19+Nef+-(Intracellular Nef Haralick variance mean$^{int/hi}$ or Nef Intensity threshold$^{int/hi}$) B cells (void)

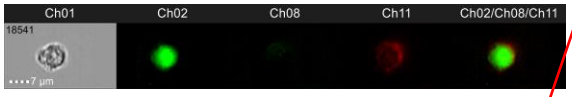

Live/Dead-CD19+Nef+-Intracellular Nef Haralick variance mean^{lo}-Nef Intensity threshold^{lo} B cells (valid)

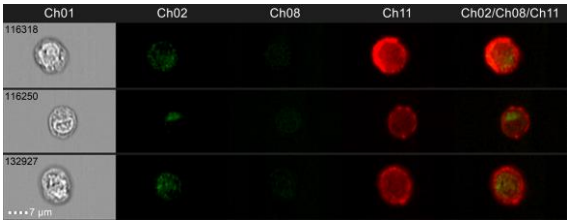

B

In vitro CD19+Nef+ B cells

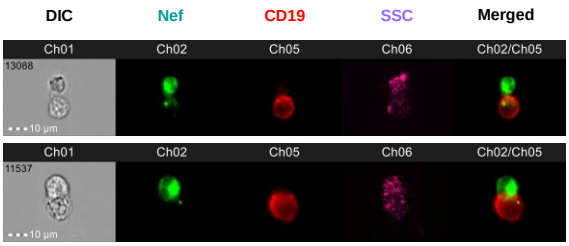

Fig. 5-Supplement 1.

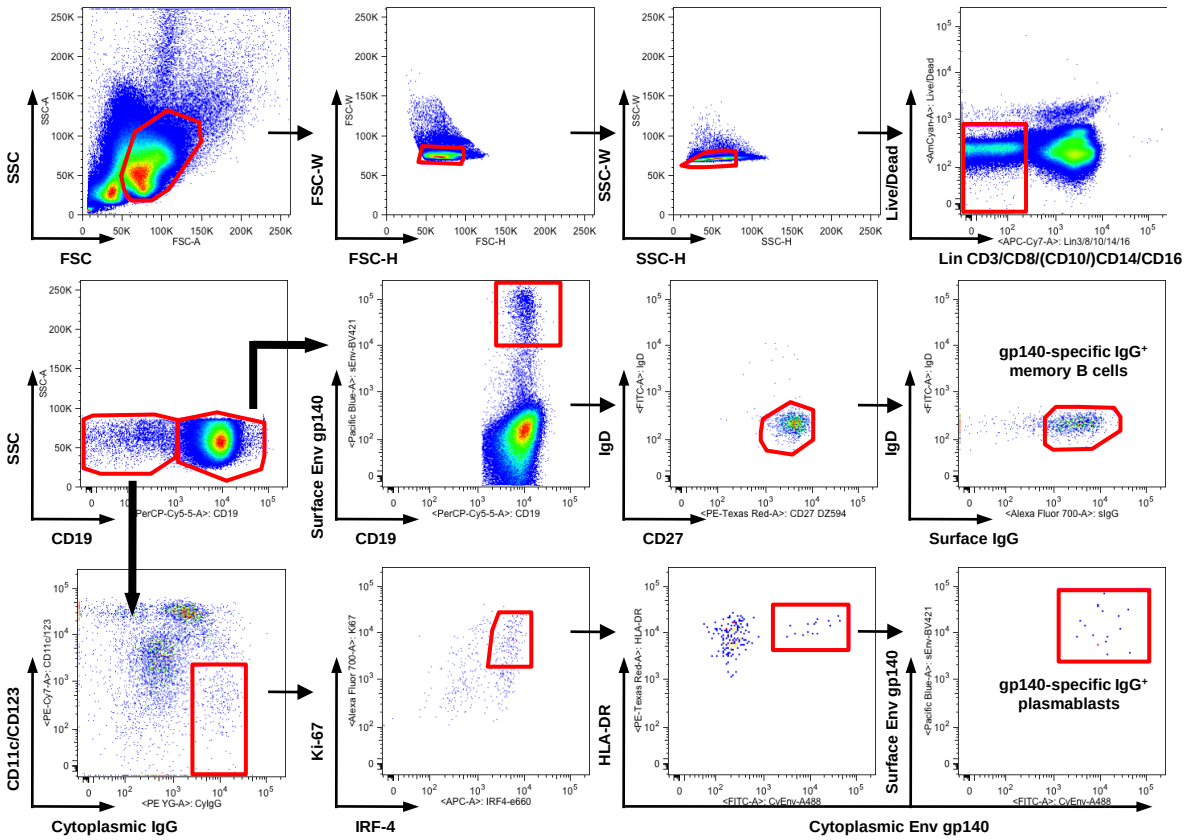

Fig. 6-Supplement 1.